J. Fluid Mech. (2002), *vol.* 466, *pp.* 365–407. © 2002 Cambridge University Press
DOI: 10.1017/S0022112002001490 Printed in the United Kingdom

Steady planar straining flow past a rigid sphere at moderate Reynolds number

By P. BAGCHI and S. BALACHANDAR

Department of Theoretical and Applied Mechanics, University of Illinois at Urbana-Champaign,
Urbana, IL 61801, USA

(Received 20 March 2001 and in revised form 8 April 2002)

This study focuses on the effect of spatial non-uniformity in the ambient flow on the forces acting on a spherical particle at moderate particle Reynolds numbers. A scaling analysis is performed to obtain conditions under which such effects are important. A direct numerical simulation, based on spectral methods, is used to compute the three-dimensional time-dependent flow past a stationary sphere subject to a uniform flow plus a planar straining flow. The particle Reynolds number, *Re*, in the range 10 to 300 covering different flow regimes, from unseparated flow to unsteady vortex shedding, is considered. A variety of strain magnitudes and orientations are investigated. A systematic comparison with the potential flow results and axisymmetric strain results is given. Under elongational strain, both the planar and axisymmetric cases are found to stabilize the sphere wake and delay the onset of unsteadiness, while compressional strain leads to instability. In terms of separation angles, length of the recirculation eddy and topology of the surface streamlines, planar and axisymmetric strains yield nearly the same results. The drag force appears to have a linear relation with strain magnitude in both cases, as predicted by the potential flow. However, contrary to the potential flow results, the drag in planar strain is higher than that in axisymmetric strain. The generation of higher drag is explained using the surface pressure and vorticity distributions. Planar strain oriented at an angle with the oncoming uniform flow is observed to break the symmetry of the wake and results in a lift or side force. The variation of the drag and lift forces may be quite complex, and unlike the potential flow results they may not be monotonic with strain magnitude. The direction of the lift force may be opposite to that predicted by the inviscid and low Reynolds number ($Re \ll 1$) theories. This behaviour is dictated by the presence or absence of a recirculation eddy. In the absence of a recirculation region at low Reynolds numbers ($Re < 20$), or at a very high strain magnitude when the recirculation region is suppressed, the results follow somewhat the pattern observed in potential flow. However, with the presence of a recirculation region, results opposite to those predicted by the potential theory are observed.

1. Introduction

The prediction of the forces acting on a particle moving in a fluid is important in many particle-laden flows. Though the problem has received attention for more than a century, many questions remain unresolved. In particular, a generalized form for the equation of motion of an individual particle that allows for both temporal and spatial variations in the surrounding flow is lacking. The effect of temporal acceleration – in the surrounding flow as well as of the particle itself – has been investigated in great detail over the past years, especially in the context of low Reynolds number and potential flows, and to some extent for finite particle Reynolds numbers. On the other hand, investigations of the effect of spatial non-uniformity in the undisturbed flow have been primarily limited to the potential flow and low Reynolds number limits. When the particle Reynolds number becomes finite, very little information is available on the nature of the flow field and the resulting forces.

One of the earliest to recognize the importance of spatial non-uniformity in the undisturbed ambient flow on the motion of a particle was Taylor (1928), who was concerned with the motion of large airships. Taylor, and later Tollmien (1938), computed the rate of change of kinetic energy of the fluid around bodies in irrotational non-uniform flows. Their investigations showed that the added-mass force acting on a stationary sphere in a steady straining flow is proportional to the pressure gradient measured at the centre of the sphere. Taylor also performed wind tunnel experiments to confirm the inviscid theory in predicting the correct equilibrium position of bodies of different shapes in converging, diverging and curved flows. Over the years Taylor's work has been revisited and generalized by others including Voinov, Voinov & Petrov (1973), and Auton, Hunt & Prud'homme (1988).

In the limit of zero Reynolds number, the unsteady motion of a particle is governed by the classical Basset–Boussinesq–Oseen (BBO) equation (Maxey & Riley 1983). In this limit the effect of quadratic variation in the undisturbed ambient flow appears as the Faxén correction (Gatignol 1983). It was shown by Saffman (1965) in his celebrated work that the shear-induced lift force can be obtained only by considering the viscous and inertial effect together at small but non-zero Reynolds number. Over the years, Saffman's work has been extended in many ways. An interesting review on the subject is given by Stone (2000). Flows other than shear have also received attention in the limit of small but non-zero Re; e.g. pure straining flow by Bedeaux & Rubi (1987), pure rotational flow by Herron, Davis & Bretherton (1975) and Weisenborn (1985), and combined rotational and straining flow by Pérez-Madrid, Rubi & Bedeaux (1990).

Investigation of the effects of non-uniform ambient flow at moderate Re ($\geqslant 1$) has been limited. In most applications, such effects are not taken into consideration due to the introduction of additional parameters as well as the significantly increased cost of computation. Hence, the results of uniform ambient flow are taken for granted. This approach is indeed valid for particles of size much smaller than the smallest relevant flow scale (for example, Kolmogorov length scale), such that the ambient flow variation over one particle diameter is much smaller than the relative velocity $\boldsymbol{U}_r$. However, as the flow variation over a particle diameter becomes comparable to $\boldsymbol{U}_r$, the effect cannot be ignored. The numerical simulations of Magnaudet, Rivero & Fabre (1995) for axisymmetric straining flow and of Dandy & Dwyer (1990) and Kurose & Komori (1999) for linear shear flow have shown that even a 10% variation in the ambient flow over a particle diameter can have a significant effect.

As in the previous investigations, in this paper we will restrict our attention to linearly varying flows. In other words, the undisturbed flow $\boldsymbol{U}(\boldsymbol{x})$ is expanded only up to $\nabla \boldsymbol{U}$ such that $\boldsymbol{U}(\boldsymbol{x}) \approx \boldsymbol{U}(\boldsymbol{x}=0) + \boldsymbol{x} \cdot \nabla \boldsymbol{U}|_{x=0}$. A particle is located at $\boldsymbol{x}=0$ and the velocity of the particle is denoted by $\boldsymbol{V}$, such that the relative velocity of the flow is given by $\boldsymbol{U}_r = \boldsymbol{U}(\boldsymbol{x}=0) - \boldsymbol{V}$. Such a linearization can be considered appropriate provided the flow variation over d is small but not negligible. Of course, for a particle size greater than the scale of the ambient flow, the problem can be quite complex. The force on the particle cannot be parameterized completely in terms of $\boldsymbol{U}_r$ and $\nabla \boldsymbol{U}|_{x=0}$ alone, and higher-order gradients of $\boldsymbol{U}$ will be required.

In this paper, we will investigate the effect of a planar straining flow on the forces acting on a stationary spherical particle. Thus our work complements the investigation of Magnaudet *et al.* (1995), who considered the effect of axisymmetric strain. Axisymmetric strain is appropriate for particles in nozzles, in pipe flows with sudden expansion or contraction and in axisymmetric jets. On the other hand, planar strain will be appropriate in the case of planar nozzles, in sudden planar expansion or contraction and in planar jets. The effect of such a large-scale mean flow gradient is relevant, for example, in the motion of airships and underwater vessels. Apart from the mean flow effect, the local turbulent velocity gradient can also play a role in determining particle forces. There is ample experimental and computational evidence to suggest that particles tend to accumulate in regions of high strain and to avoid regions of high vorticity (Wang & Maxey 1993; Elghobashi & Truesdell 1992; Squires & Eaton 1991). Furthermore, studies on turbulent structure (isotropic turbulence: Ashurst *et al.* (1987), convective turbulence: Balachandar (1992)) indicate that regions of local strain are more likely to be planar than axisymmetric. Thus there is sufficient interest in the investigation of particles subjected to planar strain.

The uniform relative motion, $\boldsymbol{U}_r$, of an undisturbed ambient flow is characterized in terms of the particle Reynolds number, $Re = |\boldsymbol{U}_r| d/\nu$. With the inclusion of a superimposed straining flow, additional parameters are required. The strength of the straining motion is measured in terms of the variation in $\boldsymbol{U}$ over a particle diameter compared to $\boldsymbol{U}_r$. The nature of the straining flow can be varied systematically from planar strain to axisymmetric strain. The orientation of the principal axes of the strain-rate tensor relative to the direction of $\boldsymbol{U}_r$ can also be varied. The present investigation covers a Reynolds number range of 10 to 300, thus extending from steady unseparated flow to periodic shedding of wake vortices, in the strain-free case. Consistent with the findings of Magnaudet *et al.* (1995), even a modest planar strain has a strong influence on the flow structure around the particle. The elongational axis of strain being aligned with the direction of $\boldsymbol{U}_r$ tends to suppress the wake, and at sufficient strain magnitude the recirculation region is completely eliminated. On the other hand, the compressional alignment of strain results in severe instability of the wake. The presence or absence of a recirculation region in the wake is likely to have a strong influence on the behaviour of the drag and lift forces. When the wake region is completely suppressed, these forces follow the same pattern found in potential flow. However, with the presence of the wake, their influence can be quite complex. In this regard the structure of the wake is quite important in understanding the forces acting on the particle.

This paper will focus on the effect of planar strain on the structure of the wake. One important difference between axisymmetric and planar strain is that under planar strain the flow is three-dimensional even in the absence of unsteadiness in the wake. Azimuthal variation in the flow, and correspondingly an azimuthal component of the flow, exist at all *Re*. Of course, as *Re* increases the flow becomes unsteady with vortex shedding, resulting in a time-dependent three-dimensional flow, even in the absence of imposed strain. In order to properly resolve the flow details and to accurately predict the lift and drag forces it is important to have a high-resolution three-dimensional and time-dependent numerical methodology. Here we employ a Fourier–Chebyshev pseudo-spectral (collocation) method, which is described in § 3. The effect of strain on the structure of the wake and the surface distribution of pressure and shear stress will be considered in § 4. In that section we will also study the resulting lift and drag forces and compare them with the potential flow prediction. Discussion and conclusions will be presented in § 5.

2. Scaling analysis

The primary effect of a non-uniform irrotational ambient flow is to introduce an added-mass force arising from convective acceleration. This inertial force is analogous to the added-mass force arising from the temporal acceleration of either the particle or the surrounding flow. The added-mass and Basset history forces due to particle acceleration are often neglected for the case of large particle to fluid density ratio. In contrast, the results on particle force in straining flows (Taylor 1928; Magnaudet *et al.* 1995) suggest that the inertial force due to ambient non-uniformity is independent of the density ratio. The purpose of this section is to establish conditions under which ambient non-uniformity would be important.

Consider the general case of a freely moving particle (droplet or bubble) at finite Reynolds number in an otherwise irrotational ambient flow. An appropriate starting point for the analysis is a semi-empirical equation for the force on the particle (Magnaudet & Eames 2000) expressed as

$$\boldsymbol{F} = \boldsymbol{F}_{\mathrm{sv}} + m_f \frac{\mathrm{D}\boldsymbol{U}}{\mathrm{D}t} + m_f C_M \left(\frac{\partial \boldsymbol{U}}{\partial t} - \frac{\mathrm{d}\boldsymbol{V}}{\mathrm{d}t} \right) + m_f C_M \boldsymbol{U} \cdot \nabla \boldsymbol{U}$$
$$+ \tfrac{3}{2} d^2 \sqrt{\pi \rho_f \mu} \int_{-\infty}^{t} K(t,\tau) \frac{\mathrm{d}(\boldsymbol{U}-\boldsymbol{V})}{\mathrm{d}\tau}\, \mathrm{d}\tau, \qquad (2.1)$$

where the fluid velocity $\boldsymbol{U}$ and its spatial and temporal derivatives are evaluated at the particle position. Here m_f is the mass of the fluid displaced by the particle and $\mathrm{D}/\mathrm{D}t$ and $\mathrm{d}/\mathrm{d}t$ are the total derivatives following a fluid element and the particle, respectively. The first term is the Stokes-like viscous force appropriate for finite Re and the second term is the pressure gradient force. The third term accounts for the added-mass effect arising from the temporal acceleration of the particle and the undisturbed flow. Here C_M is the added-mass coefficient. The fourth term is the added-mass force arising from convective acceleration. The last term is the Basset history force, which accounts for the viscous effect of unsteadiness. The history kernel $K(t,\tau)$ is proportional to $(t-\tau)^{-1/2}$ over a short time as derived by Basset, whereas at longer time it decays much faster as shown by Mei & Adrian (1992) and Lovalenti & Brady (1993).

Let the length and velocity scales of the ambient flow be denoted by L and U_0. For simplicity consider the only time scale of the ambient flow to be L/U_0. If initial transient effects are ignored, it is reasonable to take the particle velocity $\boldsymbol{V}$ and the relative velocity $\boldsymbol{U}_r$ both to scale as U_0. The characteristic time scale for particle motion is the particle response time, $\tau_p = (\rho + C_M)d^2/(18\nu)$, where $\rho = \rho_p/\rho_f$ is the particle to fluid density ratio. The appropriate scaling for the fluid acceleration is U_0^2/L, while that for the particle acceleration is U_0/τ_p.

The order of magnitude of the inertial forces (added mass and pressure gradient) and the history forces in (2.1) compared to the leading term, $\boldsymbol{F}_{\mathrm{sv}}$, are, with contributions from the fluid and particle acceleration listed separately,

	Inertial force	History force
fluid acceleration:	$Re\dfrac{d}{L}$	$\sqrt{Re\dfrac{d}{L}}$
particle acceleration:	$\dfrac{1}{(\rho + C_M)}$	$\dfrac{1}{\sqrt{(\rho + C_M)}}$

The following observations can be made from the above list. Particle acceleration follows the expected scaling: a heavy particle ($\rho \gg 1$) accelerates slowly and therefore its effect on the added-mass and history forces is negligible. In contrast, the inertial and history forces arising due to the fluid acceleration are independent of the density ratio ρ and depend only on $Re\, d/L$. For $Re\, d/L < 1$, the history force is more important than the inertial force, which is in agreement with the scaling argument presented in Mei (1990). However, at finite *Re* a faster decay of the history kernel reduces the importance of the history force at higher *Re*. In contrast, the inertial forces are important in this limit. Thus, if the particle Reynolds number and the ambient flow variation on the scale of the particle (d/L) are of $O(1)$ the effect of ambient flow non-uniformity cannot be ignored, irrespective of the density ratio.

3. Numerical methodology

3.1. *Governing equations*

We consider a spherical particle held fixed ($\boldsymbol{V} = 0$) at the origin $\boldsymbol{x} = 0$ of an inertial frame. A particle moving at a constant speed can be considered easily, by choosing a reference frame moving along with it and letting the ambient flow be corrected for the particle velocity. The undisturbed flow $\boldsymbol{U}$ is steady, linearly varying in space and directed along the x-axis at the particle position, such that

$$\boldsymbol{U}(\boldsymbol{x}) = |\boldsymbol{U}_r|\boldsymbol{e}_x + \boldsymbol{x} \cdot (\boldsymbol{S} + \boldsymbol{\Omega}), \tag{3.1}$$

where $\boldsymbol{S}$ and Ω are the pure strain and rotational part of the velocity gradient. A perturbation field $\boldsymbol{u}'(\boldsymbol{x}, t)$ takes into account the deviations from the ambient flow due to the presence of the sphere. Hence the net flow field $\boldsymbol{u}(\boldsymbol{x}, t)$ can be written as $\boldsymbol{u}(\boldsymbol{x}, t) = \boldsymbol{U}(\boldsymbol{x}) + \boldsymbol{u}'(\boldsymbol{x}, t)$. At large distances from the particle ($\boldsymbol{x} \to \infty$), $\boldsymbol{u}(\boldsymbol{x}, t)$ approaches the undisturbed ambient flow, and on the particle surface it satisfies no-slip and no-penetration conditions.

The sphere diameter d and the magnitude of the relative velocity $|\boldsymbol{U}_r|$ are used to non-dimensionalize the variables. In the following discussion any dimensionless variable will be denoted by a tilde. The governing equations for the total velocity $\tilde{\boldsymbol{u}}(\tilde{\boldsymbol{x}}, \tilde{t})$ are given by the Navier–Stokes equations as

$$\nabla \cdot \tilde{\boldsymbol{u}} = 0, \tag{3.2}$$

$$\frac{\partial \tilde{\boldsymbol{u}}}{\partial \tilde{t}} + \tilde{\boldsymbol{u}} \cdot \nabla \tilde{\boldsymbol{u}} = -\nabla \tilde{p} + \frac{1}{Re} \nabla^2 \tilde{\boldsymbol{u}}. \tag{3.3}$$

In terms of $\tilde{\boldsymbol{u}}'$ the above equations are

$$\nabla \cdot \tilde{\boldsymbol{u}}' = 0, \tag{3.4}$$

$$\frac{\partial \tilde{\boldsymbol{u}}'}{\partial \tilde{t}} + \tilde{\boldsymbol{u}}' \cdot \nabla \tilde{\boldsymbol{u}}' + \tilde{\boldsymbol{u}}' \cdot \nabla \tilde{\boldsymbol{U}} + \tilde{\boldsymbol{U}} \cdot \nabla \tilde{\boldsymbol{u}}' = -\nabla \tilde{p}' + \frac{1}{Re} \nabla^2 \tilde{\boldsymbol{u}}'. \tag{3.5}$$

Here $\tilde{p}(\tilde{\boldsymbol{x}}, \tilde{t}) = \tilde{P}(\tilde{\boldsymbol{x}}) + \tilde{p}'(\tilde{\boldsymbol{x}}, \tilde{t})$, and $\tilde{P}(\tilde{\boldsymbol{x}})$ is related to $\tilde{\boldsymbol{U}}$ by

$$\nabla \tilde{P} = -\tilde{\boldsymbol{U}} \cdot \nabla \tilde{\boldsymbol{U}}. \tag{3.6}$$

The perturbation velocity $\tilde{\boldsymbol{u}}'$ and pressure $\tilde{p}'$ are determined by solving (3.4)–(3.5) with appropriate boundary conditions. The total flow field is then obtained by adding $\tilde{\boldsymbol{U}}$ and $\tilde{P}$ to them. The resultant force (in dimensional form) on the sphere is obtained by integrating the normal and tangential stresses on the surface:

$$\boldsymbol{F} = \int_S [-p\boldsymbol{e}_r + \tau_{r\theta}\boldsymbol{e}_\theta + \tau_{r\phi}\boldsymbol{e}_\phi] \, \mathrm{d}S. \tag{3.7}$$

The first term on the right-hand side is the pressure force, while the next two terms are the viscous force. The non-dimensional force coefficient is defined as

$$\boldsymbol{C_F} = \frac{\boldsymbol{F}}{\frac{1}{2}\rho_f|\boldsymbol{U}_r|^2\pi(d/2)^2}. \tag{3.8}$$

The component of $\boldsymbol{C_F}$ along the x-axis is the drag coefficient C_D.

3.2. *Spatial discretization*

We consider a spherical coordinate system (r, θ, ϕ) (figure 1*a*) where

$$d/2 \leqslant r \leqslant R, \quad 0 \leqslant \theta \leqslant \pi, \quad 0 \leqslant \phi \leqslant 2\pi.$$

Here R represents the boundary of the computational domain. A Chebyshev expansion is implemented in the radial direction. The Gauss–Lobatto collocation points in r are first evaluated on $[-1, 1]$ as

$$\xi_i = -\cos\left[\frac{\pi(i-1)}{N_r - 1}\right], \tag{3.9}$$

for $i = 1, 2, \ldots, N_r$, where N_r is the number of radial grid points. Then a grid stretching is used to cluster points in the shear layer near the surface of the sphere. The function used for radial stretching is given by

$$\hat{\xi} = C_0 + C_1\xi - C_0\xi^2 + C_3\xi^3, \tag{3.10}$$

$$C_1 = 0.5(-\gamma_1 + 2C_0 + 3), \quad C_3 = 0.5(\gamma_1 - 2C_0 - 1). \tag{3.11}$$

The parameters C_0 and γ_1 are used to vary the amount of stretching. The computational points in physical space are obtained using the mapping

$$r_i = \tfrac{1}{2}\hat{\xi}_i\left(\tfrac{1}{2}d - R\right) + \tfrac{1}{2}\left(\tfrac{1}{2}d + R\right). \tag{3.12}$$

The azimuthal direction ϕ is periodic over 2π, and a Fourier expansion is used along this direction. The collocation points in ϕ are computed as

$$\phi_k = 2\pi(k-1)/N_\phi \tag{3.13}$$

for $k = 1, 2, \ldots, N_\phi$, where N_ϕ is the number of grid points in ϕ. In the tangential direction θ, it is sufficient to define the variables over the interval $0 \leqslant \theta \leqslant \pi$; however, the variables are periodic over 2π, and not over π. Thus a Fourier collocation in θ can be used only with some symmetry restrictions. One may note that a scalar, the radial component of a vector, and the radial derivative of a scalar are continuous over the poles ($\theta = 0$ and π). But the tangential and the azimuthal components of a vector change sign across the poles. The tangential and azimuthal derivatives of a scalar also change sign. This is the so-called 'parity' problem in spherical geometry, and has been discussed by Merilees (1973), Orszag (1974) and Yee (1981). The problem of pole-parity does not arise if surface harmonics are used. However, spectral methods using surface harmonics require $O(N)$ operations per mode, while those based on Fourier series require only $O(\log N)$ operations. In the present study, a suitable Fourier expansion in θ is derived formally by following Shariff's (1993) approach. We start by considering a typical term in the expansion:

$$\begin{Bmatrix} \tilde{c} \\ \tilde{u}_r \\ \tilde{u}_\theta \end{Bmatrix} = \begin{Bmatrix} \alpha \\ \beta \\ \gamma \end{Bmatrix} \tilde{r}^p \exp(\mathrm{i}m\theta)\exp(\mathrm{i}k\phi), \tag{3.14}$$

where $\tilde{c}$ represents a scalar. The method requires that a scalar and the Cartesian components of a vector each independently be analytic at the poles. Such a requirement results in the following acceptable expansions:

$$\tilde{c} = \begin{cases} \sum \alpha_{pmk} T_p(\tilde{r}) \cos(m\theta) \exp(\mathrm{i}k\phi) & \text{even} \quad k \\ \sum \alpha_{pmk} T_p(\tilde{r}) \sin(m\theta) \exp(\mathrm{i}k\phi) & \text{odd} \quad k, \end{cases} \tag{3.15}$$

$$\tilde{u}_r = \begin{cases} \sum \beta_{pmk} T_p(\tilde{r}) \cos(m\theta) \exp(\mathrm{i}k\phi) & \text{even} \quad k \\ \sum \beta_{pmk} T_p(\tilde{r}) \sin(m\theta) \exp(\mathrm{i}k\phi) & \text{odd} \quad k \end{cases} \tag{3.16}$$

and

$$\tilde{u}_\theta = \begin{cases} \sum \gamma_{pmk} T_p(\tilde{r}) \sin(m\theta) \exp(\mathrm{i}k\phi) & \text{even} \quad k \\ \sum \gamma_{pmk} T_p(\tilde{r}) \cos(m\theta) \exp(\mathrm{i}k\phi) & \text{odd} \quad k, \end{cases} \tag{3.17}$$

where T_p represents the pth Chebyshev polynomial and $\mathrm{i} = \sqrt{-1}$; m and k are the wavenumbers in the θ- and ϕ-directions. Here α, β and γ are the coefficients in the expansions and are functions of p, m and k. The expansion for $\tilde{u}_\phi$ follows that of $\tilde{u}_\theta$.

The collocation points in θ are distributed as

$$\hat{\theta}_j = \frac{\pi}{N_\theta}[j - 1/2] \tag{3.18}$$

for $j = 1, 2, \ldots, N_\theta$, where N_θ is the number of grid points in θ. A grid stretching is used to cluster points in the wake region of the sphere as

$$\theta_j = \tan^{-1}\left[\frac{\sin(\hat{\theta}_j)(1 - \hbar^2)}{\cos(\hat{\theta}_j)(1 + \hbar^2) - 2\hbar}\right], \tag{3.19}$$

where $\hbar$ is the parameter that controls the degree of stretching. In the simulations to be reported here, a value of $\hbar = -0.35$ provides sufficient resolution in the sphere wake. A ϕ-projection of a typical mesh is shown in figure 1(*b*).

3.3. *Temporal discretization*

A two-step time-split method is used to advance $\tilde{\boldsymbol{u}}'$ in time. In the first step the velocity field is advanced from time level n to an intermediate level '$\star$' by solving the advection–diffusion equation

$$\frac{\tilde{\boldsymbol{u}}'_\star - \tilde{\boldsymbol{u}}'_n}{\Delta\tilde{t}} + \mathbf{NL}(\tilde{\boldsymbol{u}}'_n) = \frac{1}{Re}\boldsymbol{D}(\tilde{\boldsymbol{u}}'_\star), \tag{3.20}$$

where $\boldsymbol{D}$ and $\mathbf{NL}$ are the diffusion and nonlinear terms. This is followed by a pressure correction step

$$\frac{\tilde{\boldsymbol{u}}'_{n+1} - \tilde{\boldsymbol{u}}'_\star}{\Delta\tilde{t}} = -\nabla\tilde{p}'_{n+1}. \tag{3.21}$$

By satisfying the divergence-free condition, $\nabla \cdot \tilde{\boldsymbol{u}}'_{n+1} = 0$, a Poisson equation for pressure is obtained from (3.21) as

$$\nabla^2\tilde{p}'_{n+1} = \frac{\nabla \cdot \tilde{\boldsymbol{u}}'_\star}{\Delta\tilde{t}}. \tag{3.22}$$

The above equation is solved fully implicitly for $\tilde{p}'_{n+1}$, and the intermediate velocity $\tilde{\boldsymbol{u}}'_\star$ is then corrected by (3.21) to obtain $\tilde{\boldsymbol{u}}'$ at $(n+1)$. In the advection–diffusion step, the

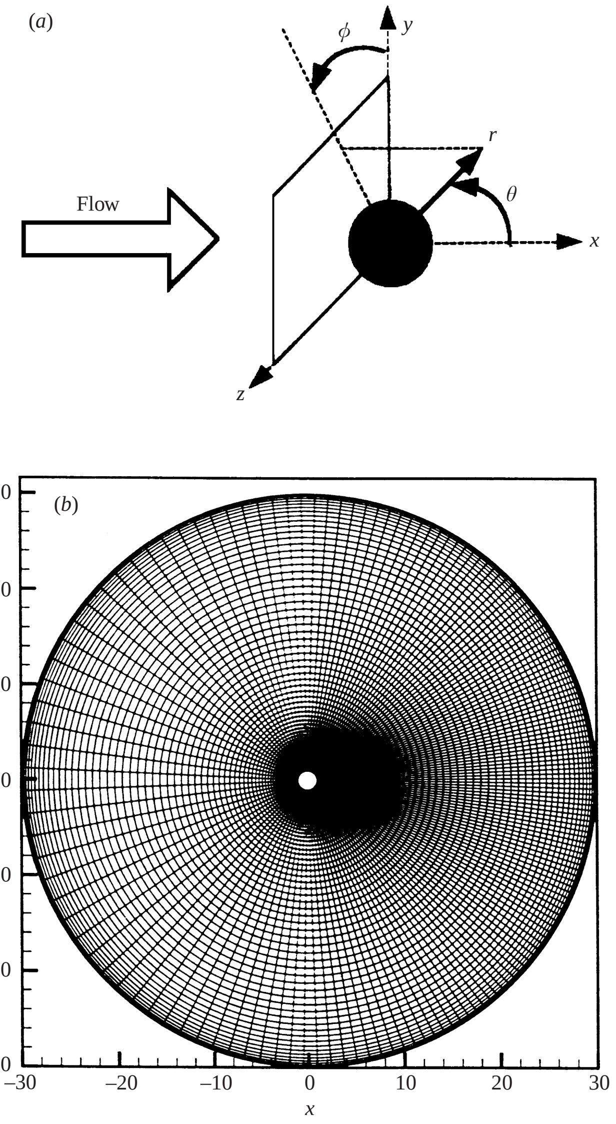

Figure 1. (a) Schematic of the spherical coordinate and (b) a ϕ-projection of the computational grid.

nonlinear and the cross-derivative terms are treated explicitly using a second-order Adams–Bashforth scheme. The θ-diffusion term is also treated explicitly. To avoid the severe viscous stability constraint due to the grid stretching near the surface, the radial diffusion term is treated implicitly using a Crank–Nicholson scheme. The azimuthal diffusion term decouples from the rest of the operators when the momentum equation is transformed to Fourier space; hence it is also treated implicitly.

3.4. *Boundary conditions*

Due to their global nature, spectral methods are extremely sensitive to boundary conditions. Only carefully derived boundary conditions will produce stable and consistent results. At the inflow, the Dirichlet boundary condition specifying an undisturbed ambient flow is used. At the outflow, a non-reflecting boundary condition by Mittal & Balachandar (1996) is used. The idea is to smoothly parabolize the governing equations by multiplying the radial diffusion terms by a filter function. The filter function is such that the diffusion terms are unaltered in most of the computational domain, while at the outflow boundary they smoothly vanish. Hence the method does not require any explicit outflow boundary condition, and the governing equations are solved there.

The radius of the outer boundary is usually taken to be 30 times the radius of the sphere. The effect of the domain size was investigated by comparing the results with those of a larger domain of size 60 times the sphere radius. For example, the drag and lift coefficients obtained from the two cases for a linear shear flow past a sphere at $Re = 100$ are 1.1183, −0.0123 and 1.1181, −0.0123, respectively, clearly implying the domain-independence of the results.

On the surface of the sphere, no-slip and no-penetration conditions are imposed for the total velocity field $\tilde{\boldsymbol{u}}$. This is equivalent to the condition that $\tilde{\boldsymbol{u}}' = -\tilde{\boldsymbol{U}}$ on the sphere surface. In the context of time-split schemes the appropriate boundary condition for the intermediate velocity is

$$\tilde{\boldsymbol{u}}'_{\star} = -\tilde{\boldsymbol{U}} + \Delta\tilde{t}(2\nabla\tilde{p}'_n - \nabla\tilde{p}'_{n-1}). \tag{3.23}$$

Combined with the homogeneous Neumann boundary condition for pressure, $\partial\tilde{p}'_{n+1}/\partial\tilde{r} = 0$, (3.23) guarantees zero penetration through the surface of the sphere, while the no-slip condition is satisfied to $O(\Delta\tilde{t}^3)$. A typical $\Delta\tilde{t}$ used in the present study is 0.001. Note that the Neumann condition for pressure is applied on the disturbance pressure $\tilde{p}'$ and not the total pressure $\tilde{p}$. The total pressure will not satisfy a Neumann condition because $\partial\tilde{P}/\partial n$ is not zero on the boundary due to the nature of the imposed straining flow.

3.5. *Pole stability*

Due to the topology of the grid, the azimuthal resolution is spatially non-uniform. The resolution is much higher near the poles than at the equator. Furthermore, the azimuthal grid spacing linearly decreases with the radial location as the surface of the sphere is approached. The viscous stability constraint due to such non-uniform resolution is avoided by the implicit treatment of the radial and azimuthal diffusion terms. However, the time-step size is still restricted by the convective stability (CFL) condition. Ideally it is desirable to have higher spatial resolution only in regions as demanded by the local flow structure. A simple strategy to remove higher ϕ resolution in regions where it is not needed is to filter high-frequency components. Such a filter necessarily has to be a function of both $\tilde{r}$ and θ.

There are some constraints that must be satisfied by the pole filter. It must be sufficiently smooth in all its variables to preserve spectral convergence. The analytic nature of the scalar and vector fields requires that in the limit $\theta \to 0$ and π, only the azimuthal modes $k = 0$ and $k = \pm 1$ exist in the expansions (3.15)–(3.17). Physically, $k = 0$ is the axisymmetric mode and it does not contribute to the pole stability constraint. The $k = \pm 1$ modes are the most unstable and lead to bifurcation in the flow (Natarajan & Acrivos 1993). Hence, to lowest order, these modes must be retained over the entire computational domain. From the CFL criterion, it can be inferred that as long as the ϕ-spectra of the velocity field decay faster than k^{-2}, the time step is dictated by the $k = \pm 1$ mode. Based on this observation, we introduce a pole filter function given by

$$f_\phi = 1 - \exp[-\lambda_1 Y^{\lambda_2}], \tag{3.24}$$

where $Y = \tilde{r}\sin\theta$. Here λ_1 and λ_2 are functions of k and are determined by the conditions

$$f_\phi = \frac{1}{k} \quad \text{at} \quad Y = Y_{\min} \quad \text{and} \quad f_\phi = 0.9 \quad \text{at} \quad Y = kY_{\min}. \tag{3.25}$$

Here $Y_{\min}$ is the value of Y at the grid point closest to the pole on the sphere (note that in (3.18) the θ discretization has been chosen to avoid $\theta = 0$ and π points). Thus the filter function attempts to achieve at least k^{-2} decay at the point closest to the pole. However, the filter function approaches unity exponentially such that at a distance $kY_{\min}$ from the pole, f_ϕ approaches 0.9. Thus filtering is localized to a very small region near the poles close to the sphere. The size of the filtered region slowly increases with the azimuthal mode number. The filter is applied on the intermediate velocity field $\tilde{\boldsymbol{u}}'_\star$ at the end of the advection–diffusion step.

4. Results and discussion

4.1. *Uniform flow*

Before presenting the results for planar straining flow we will first consider the case of uniform flow. Simulations are performed in the range $10 \leqslant Re \leqslant 500$ to cover four different flow regimes: unseparated flow for $Re < 20$, steady axisymmetric flow with separation for $20 < Re < 210$, steady non-axisymmetric flow for $210 < Re < 270$ and unsteady vortex shedding for $Re > 270$.

Up to $Re \approx 20$, the flow does not separate. But there is an asymmetry about $\theta = \pi/2$ in the vicinity of the sphere which indicates a departure from Stokes flow. The onset of separation occurs at around $Re = 20$ (Le Clair, Hamielec & Pruppracher 1970; Dennis & Walker 1971). The steady separated flow appears as an axisymmetric toroidal eddy behind the sphere. The topological structure of the wake remains the same up to $Re = 210$. At around $Re = 210$, the axisymmetric nature of the wake is broken by a regular bifurcation (Natarajan & Acrivos 1993; Tomboulides, Orszag & Karniadakis 1993). Unlike a two-dimensional bluff body, symmetry breaking in the sphere wake does not initiate the vortex shedding process and the wake remains steady for approximately $210 < Re < 270$. In this regime, the wake consists of two streamwise vortices which are opposite in sign and appear as two distinct dye threads emanating from the end of the recirculating region. It is commonly known as the 'double threaded' wake and has a plane of symmetry (the (x, y)-plane, in the present case). Figures 2(*a*) (view along the (x, y)-plane) and 2(*b*) (view normal to the (x, y)-plane) show the double threaded structure for $Re = 250$. Here the vortical structure is extracted in terms of an iso-surface of the imaginary part of the complex conjugate eigenvalues of the velocity gradient tensor (see Zhou *et al.* 1999 for details). Above $Re = 270$, the steady non-axisymmetric wake undergoes a Hopf bifurcation resulting in the periodic shedding of vortices. The hairpin-shaped vortical structures are shown in figures 2(*c*) and 2(*d*) for $Re = 350$. Even at this Re, a plane of symmetry (the x, y-plane) in the wake is present which remains fixed in time. In contrast to a two-dimensional body where vortices are shed alternately from two sides, here vortices are shed in the same orientation. The vortical structure consists of a chain of interlocking loops which is similar to the structure postulated by Achenbach (1974). The results presented here agree well with the simulations of Mittal (1999), Johnson & Patel

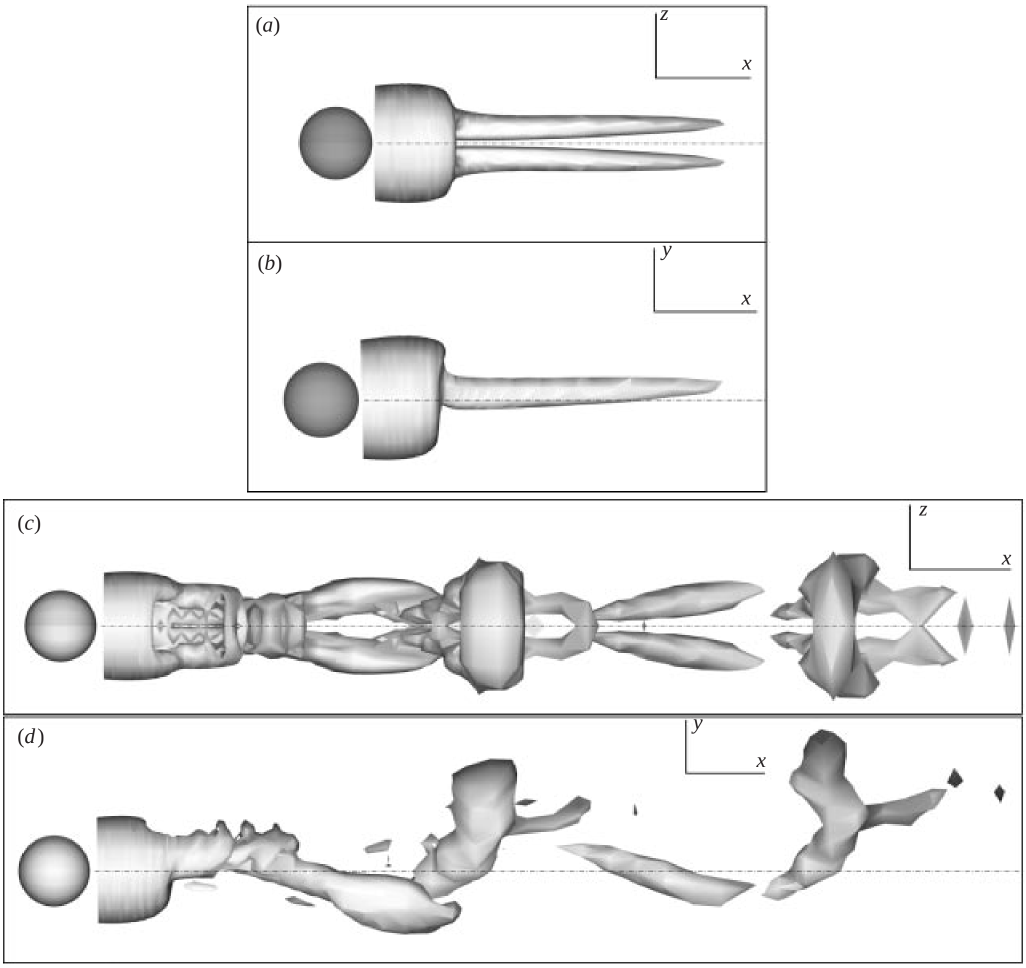

FIGURE 2. Wake structure in uniform flow. Vortical topology at $Re = 250$: (*a*) view along the plane of symmetry, (*b*) view normal to the plane of symmetry. $Re = 350$: (*c*) view along the plane of symmetry, (*d*) view normal to the plane of symmetry.

(1999), Tomboulides *et al.* (1993), and flow visualizations by Sakamoto & Haniu (1990) and Magarvey & Bishop (1961).

A quantitative comparison with previous results is shown in table 1. The drag coefficient C_D, obtained from the present simulations, agrees well with the experimental correlation of Clift, Grace & Weber (1978). Good agreement is also observed with the numerical results obtained by Mittal (1999) and Magnaudet *et al.* (1995). The separation angle, θ_s, measured from the rear stagnation point and the length of the recirculation eddy, L_e, measured from the base of the sphere and normalized by the sphere diameter are also presented for the steady regime. Here also good agreement is found with the data given in Clift *et al.* (1978) and the simulation results of Magnaudet *et al.* (1995). The separation angle and recirculation length are not reported for the non-axisymmetric and unsteady cases, as in these regimes the recirculation eddy is not a closed bubble and the separation line on the sphere surface is no longer axisymmetric. Non-axisymmetry in the wake produces a lift force, and the corresponding lift coefficient, C_L, at $Re = 250$ is found to be the same as that

	Present simulations					Previous results				
Re	C_D	C_L	θ_s	L_e/d	St	C_D	C_L	θ_s	L_e/d	St
10	4.30					4.32†				
50	1.57		40.8	0.41		1.54*, 1.57**		40.0†	0.44*	
100	1.09		53.2	0.87		1.09*, 1.09**		53.6†	0.87*	
200	0.77		63.7	1.43		0.80*, 0.765†		65.0†	1.29†	
250	0.70	−0.06				0.73*, 0.68**	−0.06‡			
350	0.62				0.135	0.64*, 0.62**				0.13–0.14¶
500	0.56				0.175	0.56*				0.17–0.18¶

TABLE 1. Comparison of the present simulations with previous experimental and numerical results for uniform flow past a sphere. * Clift *et al.* (1978); ** Mittal (1999); † Magnaudet *et al.* (1995); ‡ Johnson & Patel (1999); ¶ Sakamoto & Haniu (1995).

reported in Johnson & Patel (1999). Further comparison in the unsteady regime can be made for the dimensionless shedding frequency or the Strouhal number, $St = fd/|\boldsymbol{U}_r|$, where f is the shedding frequency. At $Re = 350$, St reported by Sakamoto & Haniu (1995) lies between 0.13 and 0.14 while Mittal's (1999) simulation predicts $St = 0.138$. These results are in reasonable agreement with the present value of 0.135. Similar agreement is found at $Re = 500$, where the present simulation predicts $St = 0.175$ against the experimental range of 0.17–0.18.

The adequacy of grid resolution can be investigated in terms of the decay of the energy spectra with respect to wavenumber. Here we present the energy spectra for a uniform flow at $Re = 500$. For this simulation a grid of $N_r = 81$, $N_\theta = 96$ and $N_\phi = 32$ points is used. The radial resolution in terms of the Chebyshev spectra, measured at two different locations in the near wake, is shown in figure 3(*a*). At least 7 orders of magnitude of decay is observed. Figure 3(*b*) shows the θ-spectra at two different radial locations: within the boundary layer, and at a downstream location far from the sphere. Here also at least 7 orders of magnitude of decay in energy is observed. The ϕ-spectra are shown in figure 3(*c*) for which a minimum decay of 9 orders is found. The chosen grid therefore provides adequate resolution for Re up to 500. Similar checks on the adequacy of resolution have been performed for all other cases, including straining flows.

Further validation of the present computational approach in linearly varying flows is given in table 2. Here we consider an axisymmetric straining flow and a linear shear flow for varying Reynolds number and dimensionless strain or shear magnitude, s (to be defined later). The drag coefficient, separation angle and recirculation length obtained from our simulations are consistent with Magnaudet *et al.*'s (1995) results for the straining flow. For the shear flow case, the drag and lift coefficients are in good agreement with the results of Kurose & Komori (1996).

The grid independence of the present results was further investigated by doubling the number of grid points in each direction to $161 \times 160 \times 64$ points. For the case of a spherical particle in a linear shear flow at $Re = 100$, $s = 0.1$, the drag and lift coefficients with increase in resolution changed from 1.118 and −0.0123 to 1.124 and −0.0126, respectively. Adequacy of resolution for other cases can be similarly verified.

4.2. *Planar strain*

In this section we will present the results for a stationary spherical particle subjected to a steady ambient flow consisting of a uniform flow and a planar straining flow.

		Present simulations					Previous results				
Imposed flow	Parameters	C_D	C_L	θ_s	L_e/d	St	C_D	C_L	θ_s	L_e/d	St
Axisymmetric strain	$Re = 100$ $s = 0.1$	1.38		42.5	0.38		1.39		43	0.37	
	$Re = 100$ $s = 0.2$	1.65		33.9	0.21		1.66		35	0.20	
	$Re = 200$ $s = 0.1$	1.07		51.3	0.57		1.06		54	0.60	
	$Re = 300$ $s = 0.1$	0.92		58.6	0.77		0.92		60	0.76	
Linear shear	$Re = 200$ $s = 0.2$	0.79	−0.058				0.80	−0.05			
	$Re = 400$ $s = 0.2$	0.62	−0.075			0.19	0.62	−0.07			0.15–0.17

TABLE 2. Comparison of the present simulations with previous numerical results for non-uniform flows over a sphere. Results for axisymmetric strain are compared with Magnaudet *et al.* (1995); results for linear shear flows are compared with Kurose & Komori (1999).

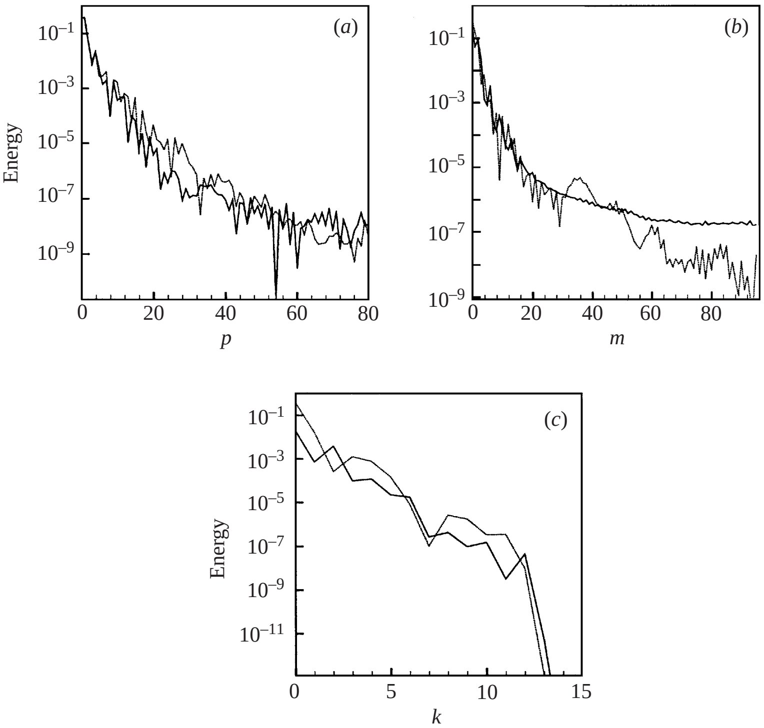

FIGURE 3. Instantaneous energy spectra along three coordinate directions at $Re = 500$. (*a*) Radial spectra at: $\theta = 0.07\pi$, $\phi = 0$ ——; and at $\theta = 0.14\pi$, $\phi = \pi$ · · · · ·. (*b*) θ-spectra at: $r = 0.75d$, $\phi = 0$ ——; and at $r = 10d$, $\phi = \pi$ · · · · ·. (*c*) ϕ-spectra at: $r = 0.75d$, $\theta = 0.07\pi$ ——; and at $r = 10d$, $\theta = 0.02\pi$ · · · · ·. The fluctuations in the spectra indicate the complex nature of the wake topology at this Reynolds number.

The results will be compared with the axisymmetric straining flow considered by Magnaudet *et al.* (1995). The uniform flow is given by the relative flow velocity at $\boldsymbol{x}=0$, and in non-dimensional terms $\tilde{\boldsymbol{U}}_r=\boldsymbol{e}_x$. The strain-rate tensor for planar strain is given by

$$\tilde{\boldsymbol{S}}=\begin{bmatrix} s\cos 2\Theta\cos^2\Phi & s\sin 2\Theta\cos\Phi & -s\cos 2\Theta\sin\Phi\cos\Phi \\ s\sin 2\Theta\cos\Phi & -s\cos 2\Theta & -s\sin 2\Theta\sin\Phi \\ -s\cos 2\Theta\sin\Phi\cos\Phi & -s\sin 2\Theta\sin\Phi & s\cos 2\Theta\sin^2\Phi \end{bmatrix}, \qquad (4.1)$$

where $\tilde{\boldsymbol{S}}=\boldsymbol{S}d/|\boldsymbol{U}_r|$, and s is the dimensionless strain magnitude. The angles Θ and Φ measure the relative orientation of the planar strain with respect to $\tilde{\boldsymbol{U}}_r$. The following orientations are considered in this study:

(*a*) elongational axis along relative velocity: $\Theta=0$ and $\Phi=0$;
(*b*) compressional axis along relative velocity: $\Theta=\pi/2$ and $\Phi=0$;
(*c*) relative velocity along the plane of strain: $\Theta\neq 0$ or $\pi/2$ and $\Phi=0$;
(*d*) relative velocity away from the plane of strain: $\Theta=0$ and $\Phi\neq 0$.

These orientations are schematically shown in figure 4. For axisymmetric strain, cases (*c*) and (*d*) are the same, whereas for planar strain they are different. In the following sections we will consider each of these cases in detail.

4.2.1. *Elongational axis along relative velocity* ($\Theta=0,\ \Phi=0$)

The influence of strain on the structure of the wake can be observed in terms of the changes in the length of the recirculation eddy, separation angle and limiting streamlines on the sphere surface. The identification of the separation line for a three-dimensional flow has been a subject of interest for many years. The issue is discussed by Tobak & Peake (1982). One way to identify the separation line is to draw the skin friction lines or the limiting streamlines from the two-dimensional vector field given by the shear stresses $\tau_{r\theta}$ and $\tau_{r\phi}$ on the surface of the sphere. For an axisymmetric flow, $\tau_{r\theta}$ and $\tau_{r\phi}$ vanish simultaneously along the line of separation, and the separation is defined as singular separation. For three-dimensional separation, a second type of separation exists in which the limiting streamlines merge together to form a separation line. For the latter type of separation, both $\tau_{r\theta}$ and $\tau_{r\phi}$ need not vanish simultaneously.

The surface streamlines for uniform flow at $Re=200$ are shown in figure 5(*a*). The view shown is the end view looking along the negative x-direction. The separation line is a perfect circle due to the steady axisymmetric nature of the wake. The unsteady non-axisymmetric regime in uniform flow is considered in figure 5(*b*) for $Re=300$. Since the flow is time-dependent, the surface streamlines in this figure correspond to an instant in the vortex shedding cycle. Here the (x,y)-plane can be identified as the plane of symmetry. Though the line of separation is nearly circular, the non-axisymmetric nature of the wake is clear from the surface streamline pattern. The separation line does not change significantly over the shedding cycle; however the rear stagnation point oscillates on the (x,y)-plane. The drag and lift forces change periodically, and the time-averaged lift remains non-zero. The effect of an axisymmetric elongational strain imposed on the uniform flow is to stabilize the flow and delay bifurcation to the non-axisymmetric and unsteady regimes. At $Re=300$, in figure 5(*c*), the axisymmetric nature of the wake is recovered under the influence of an axisymmetric strain of magnitude $s=0.1$. Consequently, the lift force is zero and the drag force remains steady in time.

The effect of planar strain on the surface streamlines is shown in figure 5(*d*) for $Re=300$ and $s=0.1$. Due to the three-dimensional nature of planar strain it is

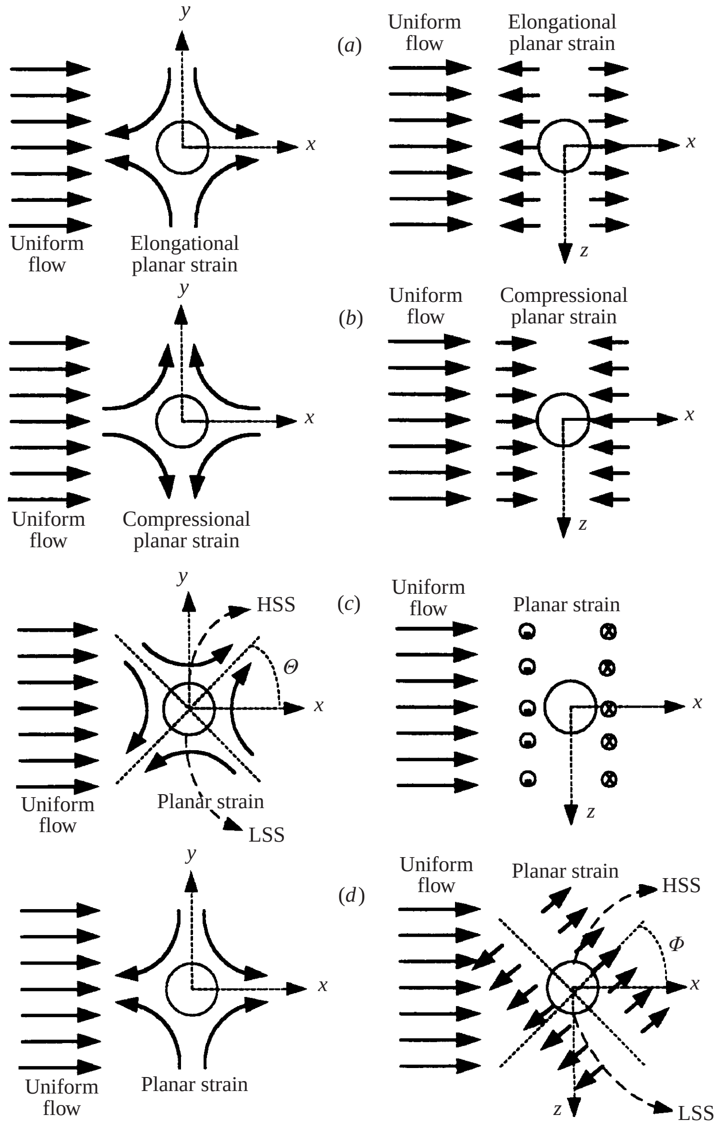

FIGURE 4. Schematic of strain orientation. The notation HSS and LSS refers to high-speed side and low-speed side of the sphere.

natural to expect the separation line to be non-axisymmetric. On the other hand, the strong favourable pressure gradient associated with elongational straining flow tends to stabilize the wake and preserve axisymmetry. The surface streamlines on the sphere appear to be strikingly similar in both the planar and axisymmetric strain cases. Similarly to the axisymmetric case, planar strain delays bifurcation to the unsteady regime. The resulting lift force in planar strain is also zero, and the drag force remains steady over time.

In axisymmetric straining flow, at moderate *Re*, the azimuthal component of velocity u_ϕ, as well as the shear stress $\tau_{r\phi}$, are zero. Thus, at any ϕ-plane, the location of separation is uniquely identified by the condition $\tau_{r\theta} = 0$. In planar strain, however,

	Plane	$s = 0$	$s = 0.05$ $(\Theta = 0)$	$s = 0.1$ $(\Theta = 0)$	$s = 0.2$ $(\Theta = 0)$	$s = 0.04$ $(\Theta = \pi/2)$
$Re = 50$	(x, y)	40.8	33.5	27.5		46.5
	(x, z)		34.2	27.2		45.5
$Re = 100$	(x, y)	53.2	46.9	41.8	34.6	58.4
	(x, z)		48.1	43.3	33.6	57.3
$Re = 200$	(x, y)	63.7	57.2	52.3	45.5	69.8
	(x, z)		58.6	53.6	45.7	69.0

TABLE 3. Effect of planar strain on separation angles. Here (x, y) and (x, z) are the planes where θ_s is measured.

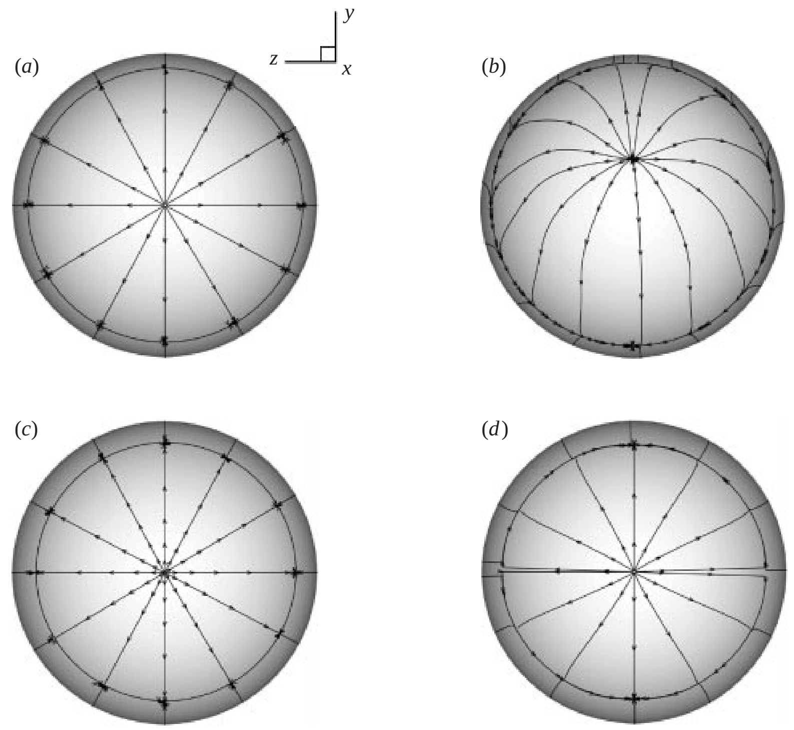

FIGURE 5. Surface streamlines for a uniform flow at (*a*) $Re = 200$, and (*b*)$Re = 300$. (*c*) Axisymmetric strain at $Re = 300$ and $s = 0.1$, (*d*) planar strain at $Re = 300$ and $s = 0.1$. Flow is directed out of the plane of the paper.

$\tau_{r\phi}$ is zero only on the (x, y)- and (x, z)-planes. Hence the condition $\tau_{r\theta} = 0$ can be used in these planes only. The difference in the separation angles in the two planes will provide quantitative information about the non-axisymmetry of the wake. Separation angles measured from the rear stagnation point are listed in table 3. The results of uniform flow $(s = 0)$ are also listed for comparison. First, we observe that the presence of an elongational strain delays the onset of separation with increasing s by imposing a favourable pressure gradient over $\theta < \pi/2$. Secondly, consistent with the nature of planar strain, separation on the (x, z)-plane occurs slightly ahead of that on the (x, y)-plane. Nevertheless, the difference between the separation angles on

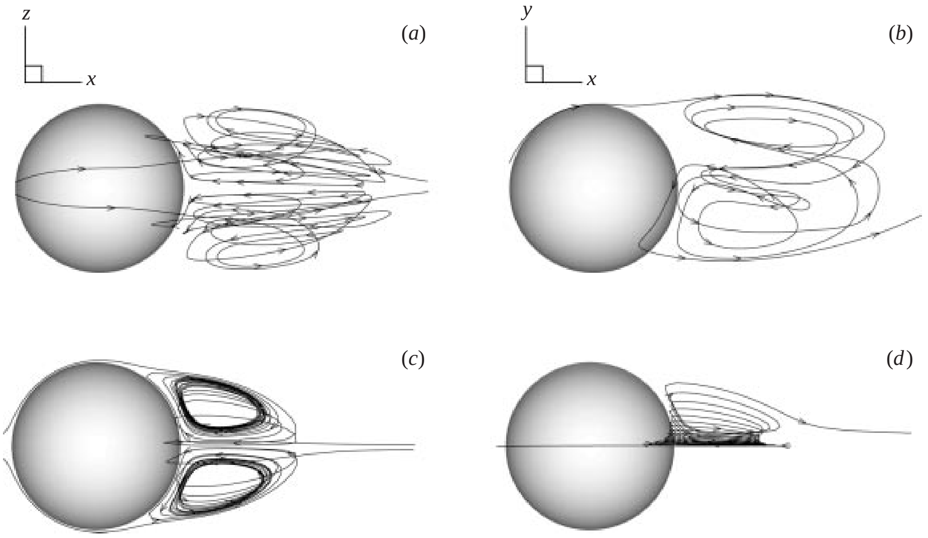

FIGURE 6. Fluid trajectory for uniform flow at $Re = 300$ (a, b) and planar strain flow at $Re = 300$ and $s = 0.1$ (c, d). The left panels (a, c) shows the view along the (x, y)-plane, and the right panels (b, d) shows the view along the (x, z)-plane.

the (x, y)- and (x, z)-planes is small, which implies that the separation line is nearly circular even in the case of planar strain. The results of the planar strain cases may also be compared with the axisymmetric strain cases given in table 2. Consistent with our observation of surface streamlines, the separation location in the case of planar strain is very close to that for axisymmetric strain.

Further insight into the non-axisymmetric nature of the wake can be gained by considering the trajectory of a fluid element. In the regime of steady axisymmetric flow, the pathlines (or streamlines) remain on individual ϕ-planes, and there is no mixing of fluid across these planes. Furthermore, the recirculation region is closed, and the fluid inside is entrapped. In the unsteady non-axisymmetric regime, the recirculation region is not closed, and there is significant mixing across different ϕ-planes. The pathlines of two fluid elements emanating symmetrically from both sides of the (x, y)-plane are shown in figure 6(a) for uniform flow at $Re = 300$. A corresponding view along the (x, z)-plane is shown in figure 6(b) where the path lines coincide. The fluid element from the upstream side is drawn around the upper focus of the recirculation eddy (located on the (x, y)-plane for $y > 0$). Then it travels around the lower focus (located on the (x, y)-plane for $y < 0$) and the upper focus several times before being ejected from the eddy and joining the downstream flow. The stable or unstable nature of the upper and lower foci alternates periodically over a shedding cycle. The pathlines are separated to the left and right of the (x, y)-plane, and there is no mixing across this plane. However, significant mixing occurs on each side of the plane.

The application of planar strain significantly affects mixing as shown in figures 6(c) and 6(d) for the case $Re = 300$, $s = 0.1$. We consider the trajectory of two fluid elements which are initially located symmetrically on either side of the (x, y)-plane. The fluid element is first drawn towards the stable foci located on the (x, z)-plane. As it spirals inwards, it is gradually pushed out of the (x, z)-plane and towards the unstable foci located on the (x, y)-plane. The pathlines in the figure indicate the direction of azimuthal velocity from one focus to the other. As the unstable foci are approached,

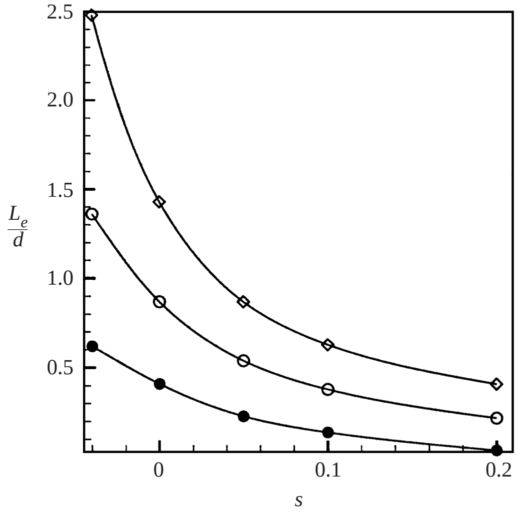

FIGURE 7. Separation length in planar strain: ●, $Re = 50$; ○, $Re = 100$; ◇, $Re = 200$.

the fluid elements begin spiralling outward and finally join the downstream flow. Note that for planar strain, both the (x, y)- and (x, z)-planes are symmetry planes. Thus fluid is confined to only one quadrant of the separation eddy resulting in less mixing. Also unlike the uniform flow case at $Re = 300$, the stable or unstable nature of the foci is fixed in time. The trajectory of the fluid elements and the nature of the foci remain similar at other Reynolds numbers and strain magnitudes as well.

The length of the recirculation region L_e normalized by the sphere diameter d is presented in figure 7. Here, L_e is measured from the sphere surface at $\theta = 0$ to the reattachment point. In elongational strain, the length decreases with higher strain magnitude; for example at $Re = 100$, $s = 0.2$, L_e/d is found to be 0.22 compared to its value of 0.87 in uniform flow. Given a strain of sufficient magnitude, the recirculation eddy may be suppressed completely as in the case of $Re = 50$, $s = 0.2$. Like the separation angles, the length of the recirculation eddy at a given Reynolds number and strain magnitude is nearly the same in both planar and axisymmetric strain (see table 2 for axisymmetric results).

For the case of elongational planar strain, the particle experiences only a drag force. The corresponding drag coefficient, C_D, is compared with the uniform flow result in figure 8(*a*). A significant increase in C_D under the influence of strain is observed. In terms of percentage change, the increase in C_D is much larger at higher Reynolds numbers. For example, at $Re = 300$ and $s = 0.2$, C_D increases by nearly 87%; on the other hand, at $Re = 10$ and for the same value of s, the increase is about 25%. The drag coefficient can be further separated into the pressure and viscous contributions, C_{PD} and C_{VD}, which are shown in figures 8(*b*) and 8(*c*). In the absence of imposed strain the pressure contribution dominates for $Re > 100$. However, over the entire range of Re, the strain-induced increase in the pressure drag is larger than that in the viscous drag. The difference is small at low Reynolds numbers, but increases substantially at higher Re.

The change in the drag coefficients with increasing strain magnitude is shown in figure 9 for $Re = 10$, 50 and 300. The variation is nearly linear with s, and a similar trend is observed at other Reynolds numbers. At $Re = 10$, the contribution from the viscous drag dominates over pressure drag, and both increase at nearly the same rate.

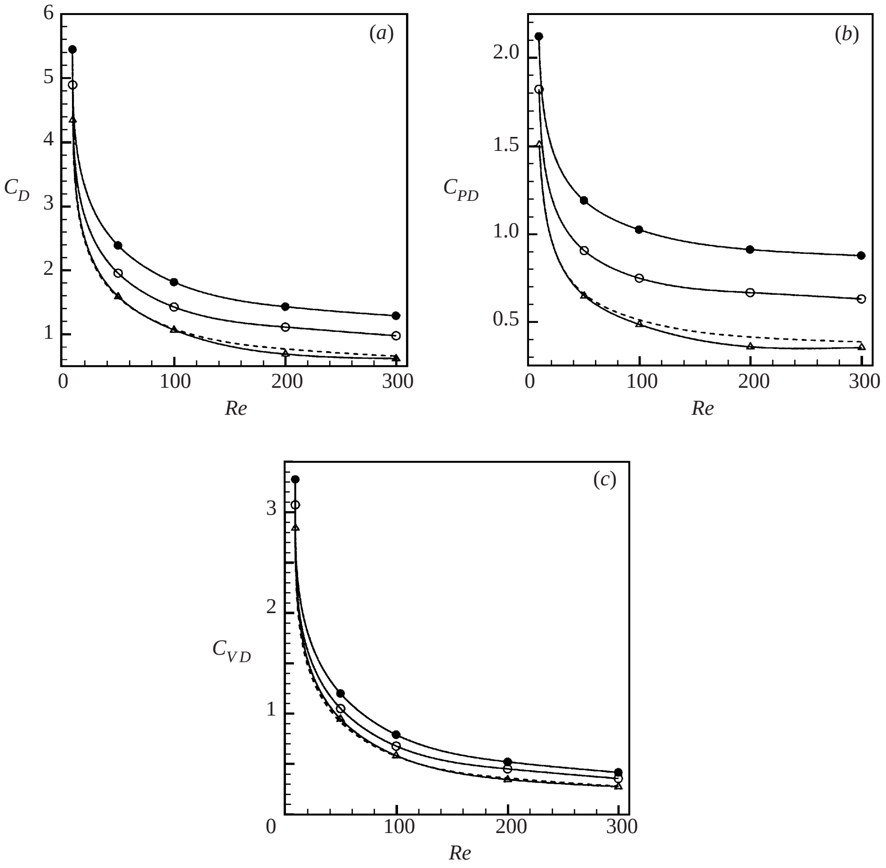

FIGURE 8. Variation of the drag coefficients with Re and s for planar strain at $\Theta = 0$ or $\pi/2$, $\Phi = 0$. (*a*) C_D; (*b*) C_{PD}; and (*c*) C_{VD}. -----, uniform flow; —○—, elongational strain ($\Theta = 0$) at $s = 0.1$; —●—, $s = 0.2$; —△—, compressional strain ($\Theta = \pi/2$) at $s = 0.04$.

At higher Re, the pressure drag increases at a faster rate than viscous drag. This effect can be clearly seen at $Re = 50$, where the viscous contribution is larger for weak strain, whereas the pressure contribution is dominant in the range $s > 0.2$. This trend continues as Re increases, and at $Re = 300$ for all s the pressure contribution dominates. From figure 9, it is clear that the drag coefficients can be expressed as the sum of two quantities: a baseline drag that corresponds to the uniform flow and a linearly increasing contribution due to strain,

$$C_D(Re, s) = A_D(Re) + B_D s, \tag{4.2}$$

$$C_{PD}(Re, s) = A_{PD}(Re) + B_{PD} s, \tag{4.3}$$

$$C_{VD}(Re, s) = A_{VD}(Re) + B_{VD} s. \tag{4.4}$$

Table 4 lists the intercept along the ordinate (A) and the slope (B) obtained from the linear fit of the data shown in figure 9. The intercept values for the total, pressure and viscous drag components are indeed very close to the corresponding values for uniform flow, i.e. $A_D(Re) \approx C_D(Re, 0)$, etc.

The above results for planar strain are qualitatively similar to those for axisymmetric strain considered by Magnaudet *et al.* (1995). The baseline total, pressure and viscous

Strain	Re	10	50	100	200	300
Planar	C_D	4.31	1.59	1.09	0.78	0.66
		(5.38)	(3.48)	(3.21)	(2.95)	(2.86)
	C_{PD}	1.51	0.662	0.51	0.42	0.38
		(2.96)	(2.37)	(2.31)	(2.26)	(2.24)
	C_{VD}	2.8	0.93	0.58	0.36	0.28
		(2.44)	(1.09)	(0.88)	(0.71)	(0.66)
Axisymmetric*	C_D	4.32		1.10	0.77	0.65
		(4.33)		(2.81)	(2.70)	(2.72)
	C_{PD}	1.49		0.51	0.40	0.37
		(2.57)		(1.96)	(2.04)	(2.08)
	C_{VD}	2.83		0.59	0.37	0.27
		(1.76)		(0.86)	(0.65)	(0.65)

TABLE 4. The y-intercepts and slopes of the best-fit linear curves for the planar and axisymmetric strain data. The values in bracket are the slopes. *, Axisymmetric data obtained from Magnaudet *et al.*'s (1995) simulations.

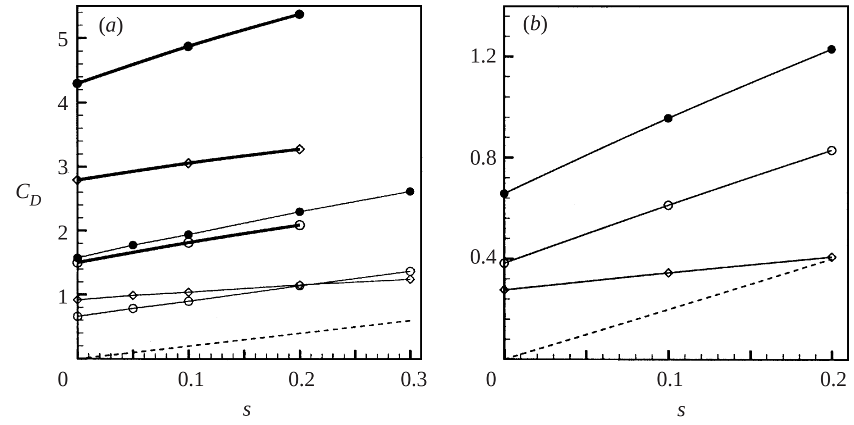

FIGURE 9. Variation of the drag coefficients with s for planar strain at $\Theta = 0$, $\Phi = 0$: (*a*) $Re = 10$ (thick lines) and $Re = 50$ (thin lines); (*b*) $Re = 300$. —●—, C_D; —○—, C_{PD}; —◇—, C_{VD}; -----, potential flow result.

drag components are nearly the same in the planar and axisymmetric cases. However, the slopes are different (see table 4). While the difference is small in the viscous contribution, it is substantial in the pressure contribution. For the planar strain cases, the values of B_{PD} and B_{VD} are somewhat higher, which implies that the drag is higher in planar strain than in axisymmetric strain.

One can use potential flow analysis as the basis for obtaining a fair comparison between the two cases. In order to do so, the dimensionless strain-rate tensor for $\Theta = 0$, $\Phi = 0$ for both axisymmetric and planar strains is written in a combined fashion as

$$\tilde{\mathbf{S}} = \begin{bmatrix} s & 0 & 0 \\ 0 & -f_s s & 0 \\ 0 & 0 & (f_s - 1)s \end{bmatrix}. \tag{4.5}$$

The parameter f_s accounts for the nature of strain; it is bounded between 1/2 (axisymmetric strain) and 1 (planar strain). The velocity potential for an ambient flow

$\tilde{\boldsymbol{U}} = \boldsymbol{e}_x + \tilde{\boldsymbol{\mathsf{S}}} \cdot \boldsymbol{x}$ can be written as

$$\left(\tilde{r} + \frac{1}{16\tilde{r}^2}\right)\cos\theta + s\left(\frac{\tilde{r}^2}{2} + \frac{1}{96\tilde{r}^3}\right)\left(\tfrac{3}{2}\cos^2\theta - \tfrac{1}{2}\right)$$
$$+ s\left(\tfrac{1}{2} - f_s\right)\left(\frac{\tilde{r}^2}{4} + \frac{1}{192\tilde{r}^3}\right)\sin^2\theta\cos 2\phi. \qquad (4.6)$$

The first term is due to the uniform flow, and the remaining terms represent contributions from strain. Using the Bernoulli equation, the pressure coefficient on the surface of the sphere is evaluated as

$$C_p = 1 - \left[-\tfrac{3}{2}\sin\theta + \tfrac{5}{12}s\left(\tfrac{1}{2} - f_s\right)\sin 2\theta\cos 2\phi - \tfrac{5}{8}s\sin 2\theta\right]^2$$
$$- \left[\tfrac{5}{6}s\left(\tfrac{1}{2} - f_s\right)\sin\theta\sin 2\phi\right]^2. \qquad (4.7)$$

The above surface pressure distribution yields a drag coefficient of $2s$, which is, surprisingly, independent of the planar or axisymmetric nature of strain. This behaviour is also implied in the inviscid analyses of Taylor (1928) and Auton *et al.* (1988). Therefore, for potential flow the only quantity that matters is the strain magnitude s, which can be interpreted as the component of $\tilde{\boldsymbol{\mathsf{S}}}$ along relative velocity. The exact partitioning of the strain-rate tensor along the other two directions does not matter. A comparison of the numerical results for the planar and axisymmetric strain cases presented in table 4 shows that this lack of dependence on the nature of strain for potential flow does not extend to finite Reynolds numbers. For the same s, planar strain results in larger drag. One possible explanation could be that the overall strain magnitude, measured in terms of $\sqrt{\mathrm{tr}(\tilde{\boldsymbol{\mathsf{S}}}^2)}$, is larger for planar strain than for axisymmetric strain.

The influence of strain on the pressure drag can be illustrated further by looking at the distribution of the pressure coefficient, C_P, on the surface of the sphere. For the uniform flow and axisymmetric strain cases, the pressure distribution is independent of the azimuthal angle, ϕ. For the case of planar strain, pressure is non-axisymmetric, and hence C_P at selected ϕ-planes will be considered. For the latter case, it is also convenient to use a ϕ-averaged pressure coefficient defined as

$$\langle C_P \rangle = \frac{1}{2\pi}\int_0^{2\pi} C_P \, \mathrm{d}\phi. \qquad (4.8)$$

First, we will consider the surface pressure distribution in potential flow. Six different curves are shown in figure 10(a) that correspond to a uniform flow case and to planar and axisymmetric strain cases, both at $s = 0.2$. For the planar strain case, C_P at three different ϕ-planes, $\phi = 0, \pi/4$ and $\pi/2$, and $\langle C_P \rangle$ are plotted. The front stagnation pressure is used as reference. The pressure distribution is symmetric about $\theta = \pi/2$ in the uniform flow case resulting in zero drag. The effect of strain is to introduce a fore–aft asymmetry about $\theta = \pi/2$ which produces a finite drag. The decrease in favourable pressure gradient on the upstream side is somewhat slowed down, but the region of favourable pressure gradient extends into the leeward side. In the case of planar strain, the effect is largest along $\phi = 0$ and smallest along $\phi = \pi/2$. The difference between $\langle C_P \rangle$ for planar and axisymmetric strains is of $O(s^2)$ and is indistinguishable in the figure.

The surface pressure distribution for $Re = 100$ is shown in figure 10(b). Five different curves are plotted: C_P for uniform flow, and for axisymmetric strain at $s = 0.2$; C_P along $\phi = 0$ and $\pi/2$ and $\langle C_P \rangle$ for planar strain at $s = 0.2$. On the

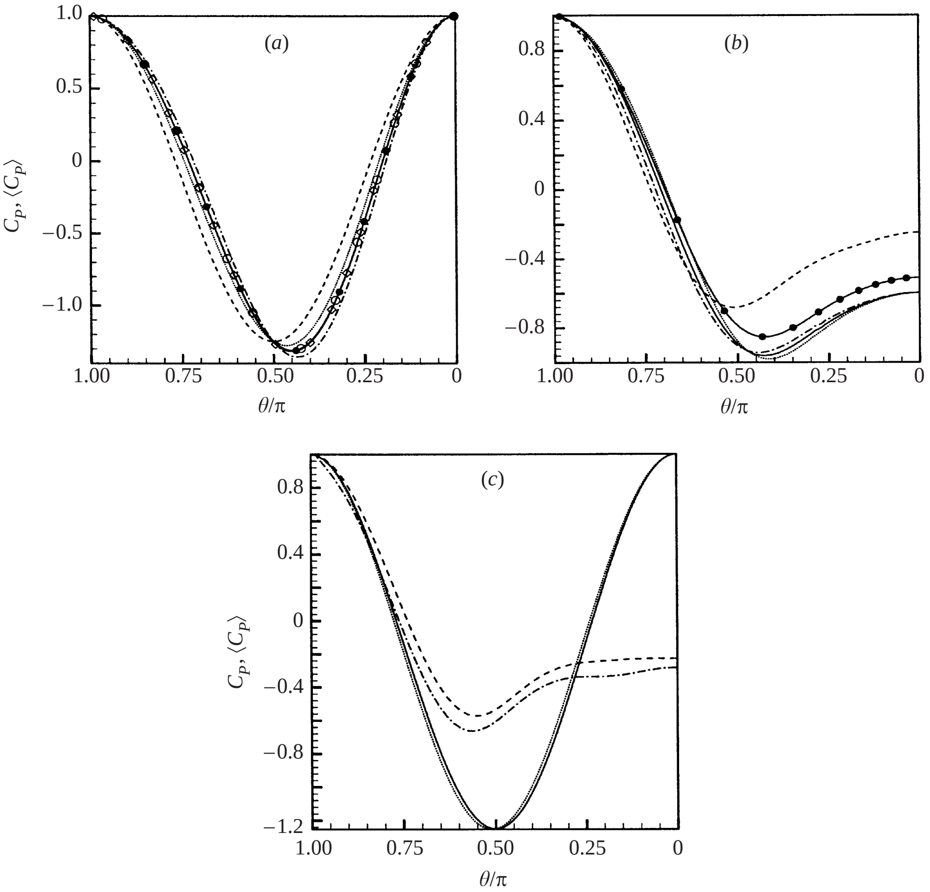

FIGURE 10. (a,b) Surface pressure distribution for the case $\Theta = 0$, $\Phi = 0$. (a) Potential flow solutions: -----, uniform flow ($s = 0$); —○—, axisymmetric strain at $s = 0.2$; —●—, ϕ-average surface pressure $\langle C_P \rangle$ in planar strain at $s = 0.2$; C_P at different ϕ-locations in planar strain: -·-·-·, $\phi = 0$; —◇—, $\phi = \pi/4$; · · · · ·, $\phi = \pi/2$. (b) $Re = 100$: -----, uniform flow ($s = 0$); —●—, axisymmetric strain at $s = 0.2$; ———, $\langle C_P \rangle$ for planar strain ($s = 0.2$); · · · · ·, C_P along $\phi = 0$ and -·-·-·, C_P along $\phi = \pi/2$ in planar strain. (c) Compressional ($\Theta = \pi/2$) strain: ———, potential flow, $s = 0$; · · · · ·, potential flow at $s = 0.04$; ----, $Re = 300$, $s = 0$; -·-·-, $Re = 300$, $s = 0.04$.

windward side, similarly to potential flow, the effect of strain is to slow down and prolong the favourable pressure gradient. On this side, difference between the two strain cases is small. However, significant difference exists on the leeward side. The wake pressure is lower in planar strain than in axisymmetric strain which results in a higher pressure drag for the former case.

Unlike the pressure drag, the viscous drag has no analogue in potential flow. We will consider variation of surface vorticity to study the effect of strain on the viscous drag. In a three-dimensional flow field, there are two orthogonal components of surface vorticity: the tangential component, ω_θ, and the azimuthal component, ω_ϕ. Under steady flow conditions, $\omega_\theta = 0$ in the case of axisymmetric strain, whereas, in planar strain, the ϕ-averaged tangential vorticity $\langle \omega_\theta \rangle$ is zero. Hence the ϕ-averaged azimuthal vorticity $\langle \omega_\phi \rangle$ alone can be used to illustrate the effect of planar strain on vorticity, and on the viscous drag. The distribution of $\langle \omega_\phi \rangle$ is shown in figure 11(a) for $Re = 10$. Three different cases are considered: uniform flow, axisymmetric strain at $s = 0.1$ and planar strain at $s = 0.1$. Corresponding results for $Re = 300$ are shown in figure 11(b). There are two different mechanisms that influence the distribution of surface vorticity under a straining flow. First, in addition to the uniform flow, the imposed strain field must also satisfy the no-slip condition. As a result, for an elongational strain, the surface vorticity from the strain component is opposite to that arising from the uniform flow on the upstream side ($\theta > \pi/2$); on the downstream side ($\theta < \pi/2$), ahead of flow separation the two contributions are of the same sign. Although the effect of strain is to shrink the separated region, the strength of the recirculation eddy is enhanced as indicated by the increased magnitude of surface vorticity in the wake. This corresponds well with the enhancement of viscous drag in the presence of elongational strain. The second mechanism leading to a change in vorticity distribution is the strain-induced vortex stretching mechanism. This mechanism also causes the magnitude of the surface vorticity to increase for $\theta < \pi/2$ and decrease for $\theta > \pi/2$. Thus the overall effect of strain is to increase viscous drag. As observed in table 4, the effect is strong in planar strain at low Re. With increasing Re, the effect is nearly independent of the nature of the strain.

4.2.2. *Compressional axis along relative velocity* ($\Theta = \pi/2$, $\Phi = 0$)

In this section we present the results of a compressional planar strain imposed on a uniform flow; in other words we consider the case $\Theta = \pi/2$, $\Phi = 0$ as shown in figure 4(b). Magnaudet *et al.* (1995) have studied the same configuration for axisymmetric strain. It is observed that the vorticity generated on the surface of the sphere is intensified as it convects along the streamwise direction. The undisturbed flow, $\boldsymbol{U}$, has a stagnation plane downstream of the sphere at $x = 2/s$ (for elongational strain ($\Theta = 0$) this plane is located upstream of the sphere). For the compressional planar strain case, the stagnation plane is located at $x = 1/s$. A vortical wake from the sphere approaches this stagnation plane from upstream and the irrotational ambient flow approaches the stagnation plane from downstream. Thus there is a discontinuity in vorticity at $x = 1/s$. At a low Reynolds number, this discontinuity can be diffused by viscosity; but at higher Re, the flow becomes unstable even at moderate s. Magnaudet *et al.* (1995) have discussed this problem in detail in the context of axisymmetric strain and obtained the corresponding stability domain. In the present simulations for planar strain, we simply restrict computations to two values of s: one at $s = 0.04$ for $10 < Re \leqslant 300$ and the other at $s = 0.1$ for $Re = 10$ only.

Contrary to elongational strain, the effect of compressional strain is to advance the location of separation and to increase the length of the recirculation region. Corresponding data are presented in table 3 and figure 7, where compressional strain cases are indicated by a negative value of s. Separation is found to advance more on the (x, y)-plane than on the (x, z)-plane. For example, at $Re = 50$ and $s = 0.04$, separation occurs at $\theta = 46.5°$ and $45.5°$, respectively, on the (x, y)- and (x, z)-planes as opposed to $40.8°$ in uniform flow. A significant increase in the recirculation length is also clear from figure 7. At $Re = 50$ and $s = 0.04$, the length is 0.62, while it is 0.41 in uniform flow. The influence of compressional strain is to reduce the drag force. The drag coefficient for various Re is shown in figure 8. Since the strain magnitude is small, the only distinguishable change is for $Re \geqslant 200$ for which C_D is reduced by 11%. For the case of $Re = 10$, $s = 0.1$, a 20% decrease in C_D is observed (not shown in the figure).

The variation of $\langle C_P \rangle$ is shown in figure 10(c) for potential flow and for the case $Re = 300$, $s = 0.04$. Under compressional strain, the region of favourable pressure

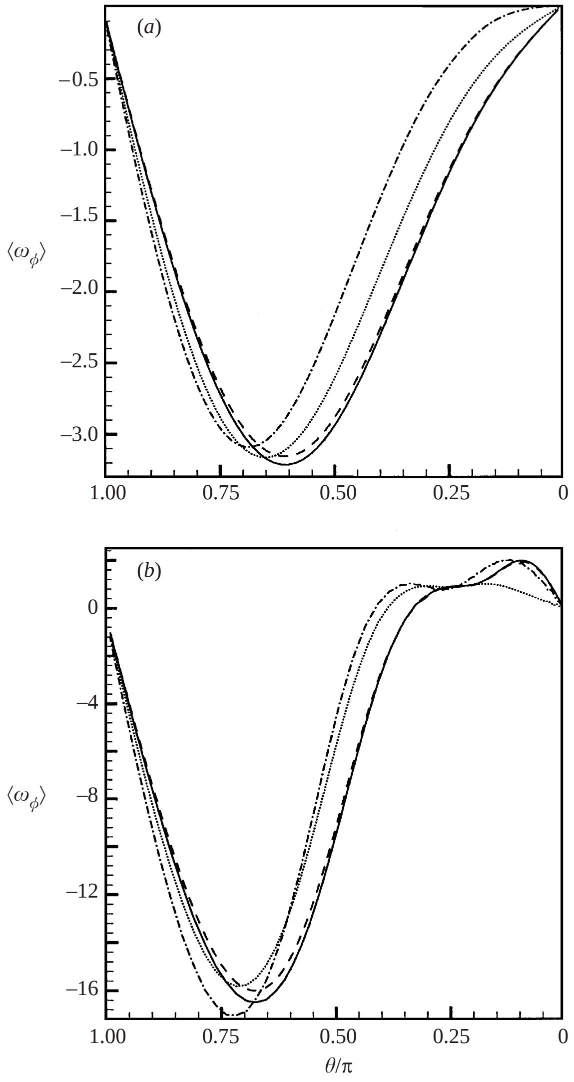

FIGURE 11. ϕ-averaged surface vorticity distribution for (*a*) $Re = 10$ and (*b*) $Re = 300$: ·····, uniform flow ($s = 0$); -----, axisymmetric strain at $s = 0.1$; ———, elongational ($\Theta = 0$) planar strain at $s = 0.1$; -·-·-·-, compressional ($\Theta = \pi/2$) planar strain at $s = 0.1$ (for $Re = 10$) and $s = 0.04$ (for $Re = 300$).

gradient is reduced. The decrease in pressure drop in the windward side is also faster compared to the uniform flow case. But unlike potential flow, $\langle C_P\rangle$ at $Re = 300$ is lower even on the downstream side of the sphere. Such a decrease in $\langle C_P\rangle$ on the leeward side actually tends to increase the pressure drag. The effect is however overcome by the decrease in favourable pressure on the windward side resulting in an overall decrease in the pressure drag. A similar variation in $\langle C_P\rangle$ is observed at other Reynolds numbers as well. The average surface vorticity $\langle\omega_\phi\rangle$ for $Re = 10$, $s = 0.1$ and $Re = 300$, $s = 0.04$ is shown in figure 11. The magnitude of $\langle\omega_\phi\rangle$ decreases on the downstream side and increases on the upstream side which results in a decrease in the viscous drag.

The $Re = 300$, $s = 0.04$ case develops unsteady vortex shedding. The shedding process appears to be more chaotic than in uniform flow and is dominated by a low-frequency mode at $St \approx 0.035$. Although the compressional strain magnitude considered is weak, certain aspects of the flow, such as movement of the separation line and the recirculation length, seem to fit the trend observed in elongational strain. On the other hand, the behaviour of the drag coefficient cannot be extrapolated from the results of elongational strain. As observed by Magnaudet *et al.* (1995), the present approach becomes unstable for larger values of compressional strain. This raises the interesting question of whether such an ambient flow configuration is stable for an extended period of time.

4.2.3. *Relative velocity along the plane of strain* ($\Theta \neq 0$ *or* $\pi/2$, $\Phi = 0$)

This section deals with the situation where the relative velocity is in the plane of strain but not aligned along the elongational or compressional direction of strain. In particular, the case of $\Theta = \pi/4$, $\Phi = 0$ will be considered (see figure 4*c*). Along $x = 0$, $y > 0$ (the top side of the sphere), the straining flow acts in the same direction as the uniform flow, while along $x = 0$, $y < 0$ (the bottom side) it opposes the uniform flow. Thus the $y > 0$ side will be called the high-speed side (marked HSS), and the $y < 0$ side will be called the low-speed side (LSS). The effect of strain on the structure of the wake is described first. Streamlines constructed from the velocity field on the (x, y)-plane are shown in figure 12. For the given strain orientation, this is a plane of symmetry. The $Re = 10$, $s = 0.1$ case is shown in figure 12(*a*). The symmetry of the flow about the (x, z)-plane is broken, and the front and rear stagnation points are no longer located at the poles $\theta = 0$ and π. At higher *Re*, the shape of the wake is dramatically modified in the presence of strain. Figures 12(*b*) and 12(*c*) show the effect of increasing strain magnitude while *Re* is held fixed at 50. Even a relatively weak strain of $s = 0.05$ can be seen to visibly break the axisymmetric nature of the wake. The recirculation eddy is suppressed on the high-speed side, while it is reduced in size on the low-speed side. Fluid moving around the bottom of the sphere continues around the eddy and departs near the upper separation line, joining the fluid from the high-speed side. The recirculation eddy almost disappears with increasing strain magnitude, as shown in figure 12(*c*) for $Re = 50$, $s = 0.1$. At even higher strain magnitudes the separation eddy is completely suppressed. The effect of strain at higher *Re* is considered in figure 12(*d*) for $Re = 300$, $s = 0.1$. The deformation of the recirculation eddy is quite similar to that shown in figure 12(*b*). Comparing figures 12(*c*) and 12(*d*), it may be claimed that suppression of the eddy is pushed up to higher strain magnitude as *Re* increases. At $Re = 300$, $s = 0.1$, the flow is steady, thus suggesting that strain oriented at $\pi/4$ tends to inhibit the vortex shedding process.

The locations of separation on the (x, y)-plane are presented in table 5. For the case of $s = 0.1$, at all $Re \geqslant 100$, separation is advanced on the high-speed side ($\phi = 0$) and is delayed on the low-speed side ($\phi = \pi$). The effect of increasing s from 0 to 0.2 while keeping *Re* fixed at 50 is also shown in table 5. For a relatively weak strain, at $s = 0.05$, the separation line remains a closed curve, though not axisymmetric. Separation on $\phi = 0$ occurs at $\theta = 41.9°$ which is higher than the $\theta = 40.8°$ in uniform flow. Separation on $\phi = \pi$ is however delayed to $\theta = 37.9°$. When s is increased beyond 0.05, lower separation no longer exists, and upper separation is advanced further upstream. Also shown in table 5 are the locations of the rear and front stagnation points. Owing to the symmetry of the applied strain field about the (x, y)-plane, these points are confined to this plane only. However, they are no longer

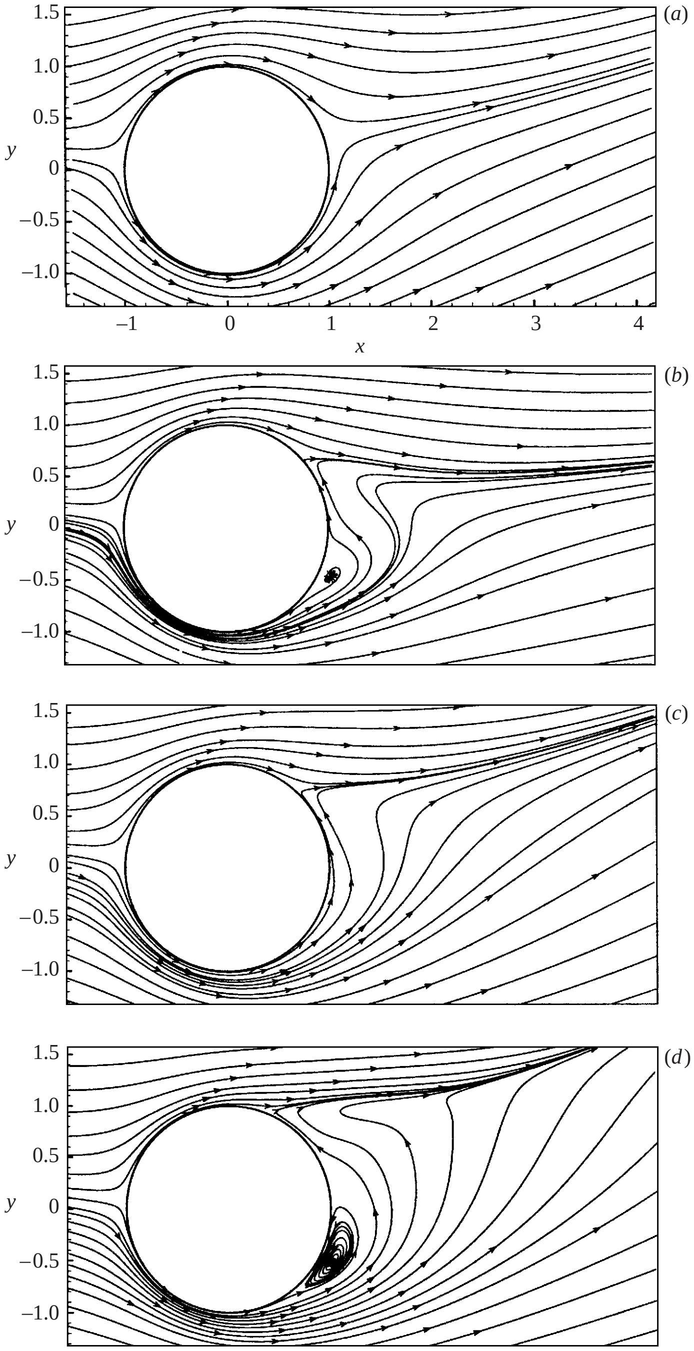

FIGURE 12. Streamline contours on the (x, y)-plane for $\Theta = \pi/4$, $\Phi = 0$. (*a*) $Re = 10$, $s = 0.1$; (*b*) $Re = 50$, $s = 0.05$; (*c*) $Re = 50$, $s = 0.1$; (*d*) $Re = 300$, $s = 0.1$.

located at $\theta = 0$ and π. For the entire range of Re and s, the front stagnation point is located nearly at the same θ on the high-speed side. The movement of the rear stagnation point is however very different. At $Re = 10$ and $Re \geqslant 200$ and $s = 0.1$, it is located on the high-speed side. But at $Re = 50$, $s = 0.05$ and $Re = 100$, $s = 0.1$, it has moved towards the low-speed side.

		θ_s		Stagnation point	
Re	s	$\phi = 0$	$\phi = \pi$	Rear	Front
10	0.1			19.2	174.3
50	0.05	41.86	37.9	7.1, on LSS	174.0
50	0.1	47.64			173.9
50	0.2	52.19			170.0
100	0.1	57.58	31.71	5.3, on LSS	173.9
200	0.1	65.66	47.94	10.6	174.2
300	0.1	69.76	54.67	19.9	174.5

TABLE 5. Location of the separation and stagnation points for $\Theta = \pi/4$, $\Phi = 0$ case.

We also examine the sphere wake by means of the surface streamline plots in figure 13. For the $Re = 50$, $s = 0.05$ case shown in figure 13(a), a downward movement of the rear stagnation point (indicated as RS in the plot) away from the geometric pole ($\theta = 0$) is clearly visible. The top–bottom asymmetry in the wake is also quite evident here. Figure 13(b) shows the surface streamlines for $Re = 50$ and $s = 0.1$. The separation line is no longer a closed curve, and it exists only on the high-speed side. With further increase in s, the separation line is gradually reduced before being eliminated completely at a sufficiently high strain. The non-axisymmetric nature of the wake can also be observed in figures 13(c) and 13(d) corresponding to the $Re = 100$, $s = 0.1$ and $Re = 300$, $s = 0.1$ cases.

A close observation of the surface streamlines reveals an interesting phenomenon. In figure 13(a), for $Re = 50$ and $s = 0.05$, all the surface streamlines merge tangentially to the separation line at the upper singular point located on the $\phi = 0$ plane, whereas only two surface streamlines intersect each other at the lower singular point at $\phi = \pi$. Thus, the upper singular point is a nodal point, denoted by N in the plot, while the lower one is a saddle point, denoted by S. At $s = 0.1$ (figure 13b), the nodal point is no longer located at $\phi = 0$. Instead, there are two nodal points (N1 and N2) located on either side of the (x, y)-plane, and a saddle point (S) appears at $\phi = 0$. The trend is further magnified at higher strain magnitudes. The effect of increasing Re is shown in the next two plots. At $Re = 100$ and $s = 0.1$, in figure 13(c), the singular points at $\phi = 0$ and π are saddle points (S1 and S2). Two nodal points (N1 and N2) are now located away from the (x, y)-plane in $y < 0$. At $Re = 300$, $s = 0.1$, in figure 13(d), two nodal points merge into the lower singular point (N) at $\phi = \pi$, while the upper singular point (S) at $\phi = 0$ still remains a saddle point.

The drag coefficient C_D for the case of $\Theta = \pi/4$ and $\Phi = 0$ is presented in figure 14(a) for $s = 0.1$. The coefficients C_D, C_{PD} and C_{VD} have nearly the same values as in uniform flow. Although there is a small increase in the coefficients over their values in uniform flow, the effect is far less than what was observed under elongational alignment. Considering potential flow for the orientation $\Theta \neq 0$ and $\Phi = 0$, the velocity potential is given by

$$\left(\tilde{r} + \frac{1}{16\tilde{r}^2}\right)\cos\theta + s\left(\frac{\tilde{r}^2}{2} + \frac{1}{96\tilde{r}^3}\right)\left(\tfrac{3}{2}\cos^2\theta - \tfrac{1}{2}\right)\cos 2\Theta$$
$$-s\left(\frac{\tilde{r}^2}{2} + \frac{1}{96\tilde{r}^3}\right)[(\sin^2\theta\cos 2\phi)\cos 2\Theta - \sin 2\theta\cos\phi\sin 2\Theta]. \quad (4.9)$$

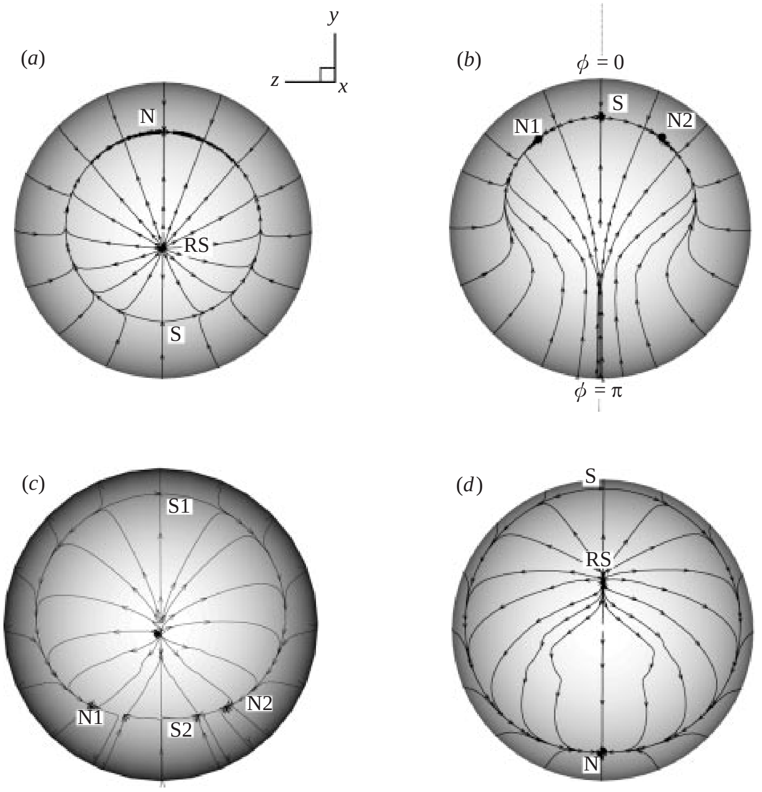

FIGURE 13. Surface streamlines for $\Theta = \pi/4$, $\Phi = 0$. (*a*) $Re = 50$, $s = 0.05$; (*b*)$Re = 50$, $s = 0.1$; (*c*) $Re = 100$, $s = 0.1$; (*d*) $Re = 300$, $s = 0.1$.

In particular, for $\Theta = \pi/4$ and $\Phi = 0$, $C_{D,\text{pot}} = 0$. Therefore the trend of a weak influence on drag observed at finite Reynolds number is consistent with the potential flow result.

The ambient flow considered here is not symmetric about the (x, z)-plane. As a result, a lift force is generated along the y-direction. For $\Theta = \pi/4$, $C_{L,\text{pot}} = 2s$, and the lift force is directed to the positive y-axis, i.e. from the low-speed side of the sphere to the high-speed side. In the limit of low Reynolds number ($Re \ll 1$) also, the lift coefficient was observed to be positive by Pérez-Madrid *et al.* (1990). The present simulations, however, show that C_L at moderate Re may be directed towards the negative y-axis. The variation of C_L and its pressure and viscous components are shown in figure 14(*b*) for a fixed strain magnitude of $s = 0.1$. Except for $Re < 40$, C_L is negative over the entire range of Re. The pressure contribution C_{PL} is negative for approximately $Re > 80$, while the viscous contribution C_{VL} is negative for $Re > 10$. The generation of a negative lift force at finite Re is contrary to the potential flow and low Reynolds number limits and therefore is somewhat surprising. However, it must be pointed out that such a negative lift force has also been observed in both experiments and computations for the case of spheres subjected to a linear shear flow by Kurose & Komori (1999).

Figure 14(*c*) presents the variation of the lift coefficients with increasing s as Re is held fixed at 50. The finite-Re behaviour is very different from the linear variation predicted by potential flow. All three lift coefficients first attain a negative maximum

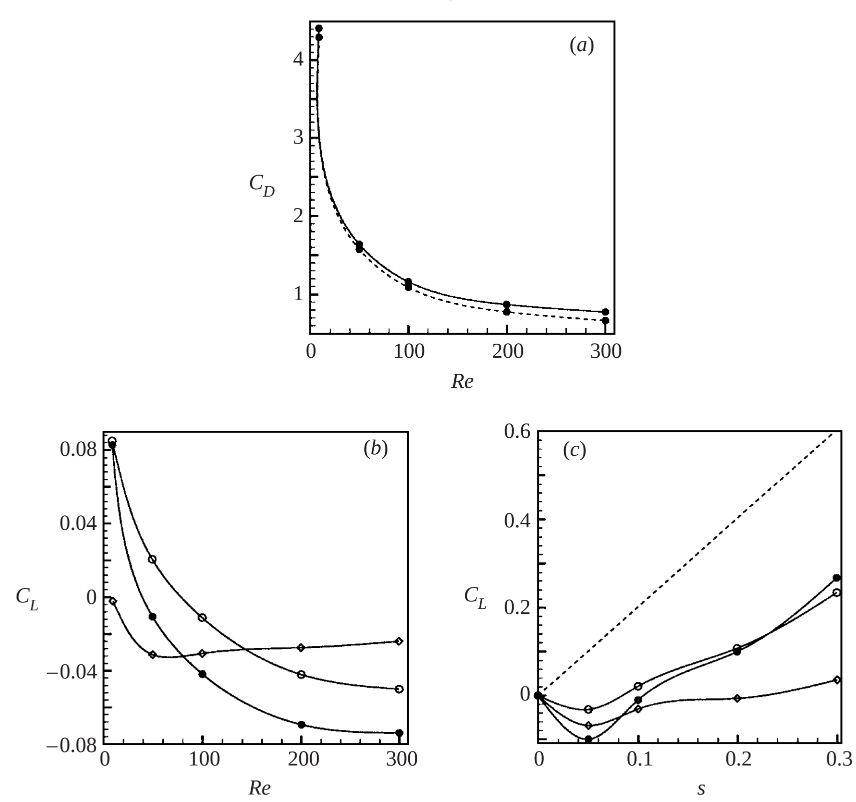

FIGURE 14. Drag and lift coefficients for $\Theta = 45°$, $\Phi = 0$. (*a*) Variation of C_D with *Re*: —●—, $s = 0.1$; --●--, strain-free uniform flow. (*b*) Lift coefficients at $s = 0.1$: ●, C_L; ○, C_{PL}; ◇, C_{VL}. (*c*) Lift coefficients at $Re = 50$: ●, C_L; ○, C_{PL}; ◇, C_{VL}. ------, potential flow result.

at about $s = 0.05$. Both C_L and C_{PL} then increase with s and eventually become positive for $s > 0.1$. The viscous part C_{VL}, however, remains negative up to about $s = 0.25$. At $s = 0.05$, the viscous lift contributes nearly 70% of the total lift, while at $s = 0.3$ it accounts for only 12%. Thus, the pressure contribution takes over the viscous contribution as *Re* and s increase.

The generation of the negative lift force is explored by considering separately the pressure and viscous contributions. The pressure coefficient C_P on the surface of the sphere is shown in figure 15 for two cases: $Re = 200$, $s = 0.1$ and $Re = 50$, $s = 0.2$. We consider the variation of C_P with θ along $\phi = 0$ and π where C_P attains extremal values. The corresponding distributions for potential flow are also shown. The potential pressure along the high-speed side is slightly larger than that along the low-speed side near $\theta = 0$ and π. However, the large drop in pressure along the high-speed side near $\theta = \pi/2$ results in a positive lift. The finite-*Re* behaviour is significantly different, especially in the wake region. For the $Re = 200, s = 0.1$ case, the pressure drop along the high-speed side is much less and C_P along $\phi = 0$ and $\phi = \pi$ is nearly the same for $\theta \leqslant \pi/2$. On the other hand, for $\theta > \pi/2$, C_P along $\phi = 0$ is higher than that along $\phi = \pi$. Therefore the negative value of C_{PL} arises essentially from the negative contribution in $\theta > \pi/2$. In figure 15(*b*), for the case of $Re = 50$, $s = 0.2$, the pressure drop on the high-speed side near $\theta = \pi/2$ is large enough to overcome the negative contribution arising from the upstream side, thereby producing a positive value of C_{PL}.

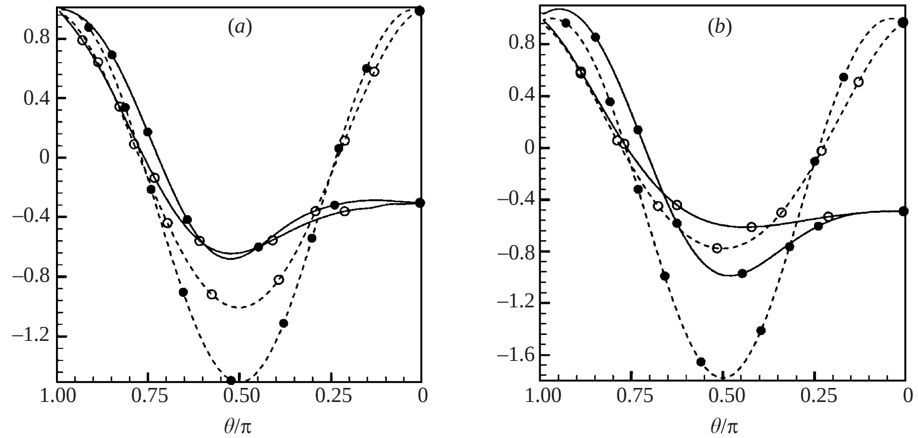

FIGURE 15. Surface pressure distribution for $\Theta = 45°$, $\Phi = 0$. (*a*) $Re = 200$, $s = 0.1$; (*b*) $Re = 50$, $s = 0.2$. ———, finite-*Re* result; - - - - - -, potential flow; ●, C_P along $\phi = 0$; ○, C_P along $\phi = \pi$.

In figure 14 it was observed that for moderate strain magnitudes in the range $0 \leqslant s \leqslant 0.3$, the pressure contribution to the lift force is generally positive at low Reynolds numbers ($Re = 10$) and negative at higher Reynolds numbers ($Re \geqslant 200$). For intermediate Reynolds numbers ($Re = 50$), the pressure contribution changes from negative at low strain values ($s \leqslant 0.1$) to positive at higher strain. This behaviour is investigated further in figure 16 where contours of the local contribution to the y-component of the pressure lift are plotted. Here the local contribution is defined in terms of the deviation in the surface pressure from its surface-averaged value. Four different cases are considered: (*a*) $Re = 10$, $s = 0.1$; (*b*) $Re = 50$, $s = 0.05$; (*c*) $Re = 50$, $s = 0.2$; and (*d*) $Re = 300$, $s = 0.1$. Owing to the symmetry of the flow about the (x, y)-plane, only one half of the surface is shown. For all cases, the behaviour near $\theta = \pi$ is similar to the potential flow result: higher than average pressure above the centreline contributing to negative lift and lower than average pressure below the centreline contributing to positive lift. The negative contribution above the centreline somewhat outweighs the positive contribution, and thus for all four cases there is a negative contribution to the pressure lift coming from the upstream portion of the sphere. However, away from the upstream side, results are markedly different for each case. For $Re = 10$, $s = 0.1$, a strong upward force is present on the downstream side, which makes the resultant contribution positive. For $Re = 50$, $s = 0.05$, the pressure on the upper surface is roughly comparable to that on the lower surface over almost the entire range of θ except near $\theta = \pi$. Near $\theta = \pi$, the negative contribution is strong enough to produce a negative pressure lift. When s is increased, as in figure 16(*c*) for $Re = 50$, $s = 0.2$, a stronger positive force acts on the top surface near $\theta = \pi/2$ resulting in a positive pressure lift. For the high Reynolds number case of $Re = 300$, $s = 0.1$ shown in figure 16(*d*), the significant pressure difference comes only from the upstream side of the sphere, and the overall pressure lift is negative.

In summary, one can conclude that when the recirculation region is absent in the wake, the pressure distribution for $\theta \leqslant \pi/2$ dictates that the pressure lift force must be positive, just as in potential flow. This situation arises at low *Re* when the recirculation region is entirely absent, or at higher *Re* when the formation of the recirculation region is suppressed by the presence of a strong straining flow. When the recirculation region is present, the wake pressures above and below the (x, z)-plane

Re	s	C_{VL} due to $\tau_{r\theta}$	C_{VL} due to $\tau_{r\phi}$
10	0.1	0.0298	−0.03
50		0.0110	−0.04
100		0.0069	−0.04
200		0.0030	−0.03
300		0.0006	−0.02
50	0.05	−0.008	−0.06
	0.1	0.011	−0.04
	0.2	0.035	−0.04

TABLE 6. Contribution of the shear stresses $\tau_{r\theta}$ and $\tau_{r\phi}$ to the viscous lift for the case $\Theta = 45°$, $\Phi = 0$.

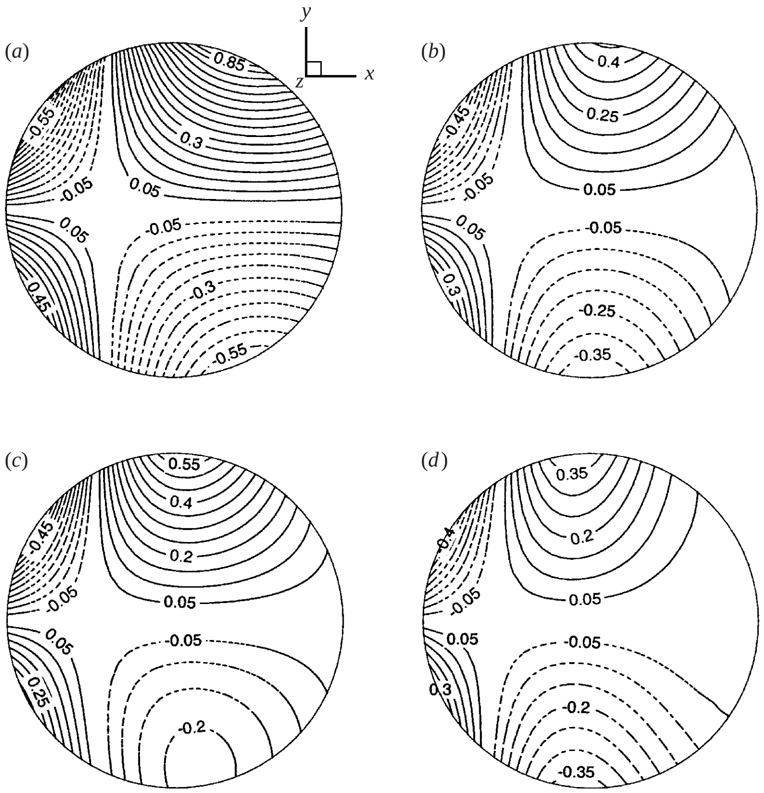

FIGURE 16. Contours of the y-component of surface pressure for $\Theta = \pi/4$, $\Phi = 0$. (*a*) $Re = 10$, $s = 0.1$; (*b*) $Re = 50$, $s = 0.05$; (*c*) $Re = 50$, $s = 0.2$; and (*d*) $Re = 300$, $s = 0.1$. Contours are plotted in steps of 0.05. The dashed lines indicate negative values.

are nearly equalized, and the resultant effect is a negative pressure lift arising from the front part ($\theta \approx \pi$) of the sphere.

The viscous lift force arising from two contributions, $\tau_{r\theta}$ and $\tau_{r\phi}$, is listed in table 6. The contribution from $\tau_{r\phi}$ is negative over the entire range of Re and s. The contribution from $\tau_{r\theta}$ is mostly positive, but nearly an order of magnitude less than that from $\tau_{r\phi}$, except at $Re = 10$ and at $Re = 50$ for high values of s.

The role of the shear stress $\tau_{r\theta}$ in the lift force is examined in figure 17. The flow is

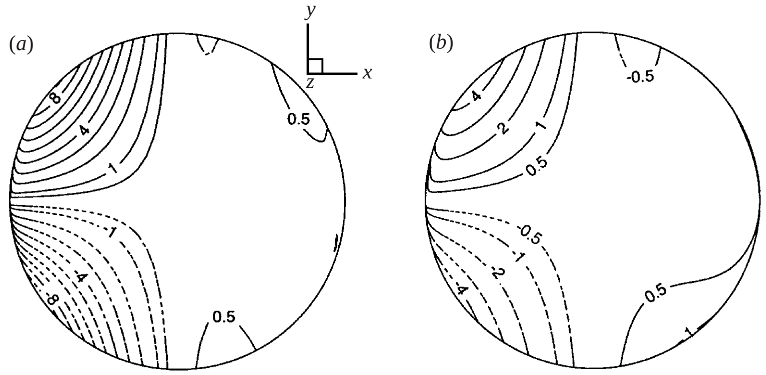

FIGURE 17. Contours of the y-component of viscous force due to the $\tau_{r\theta}$ contribution. (a) $Re = 200$, $s = 0.1$, (b) $Re = 50$, $s = 0.2$.

from left to right, and the view shown here is looking towards the negative z-axis. Here contours of the y-component of the viscous force arising from $\tau_{r\theta}$, i.e. $\tau_{r\theta}\cos\theta\cos\phi$, are shown on one half of the sphere surface. A positive value of this quantity leads to a positive viscous lift force, while a negative value contributes negatively. We consider two representative cases: (a) $Re = 200$, $s = 0.1$ and (b) $Re = 50$, $s = 0.2$. For the first case, values on the upper and lower surface of the sphere are nearly comparable but of opposite sign over the entire range of θ. Thus the integrated value of $\tau_{r\theta}\cos\theta\cos\phi$ over the surface is negligible. For the second case, values on the upper and lower surface on the upstream side of the sphere are roughly the same and of opposite sign. But a positive contribution arises from the lower surface on the downstream side of the sphere. Similarly to the surface pressure behaviour, the effect of $\tau_{r\theta}$ is dictated by the presence of a recirculation eddy. In the case of $Re = 200$, $s = 0.1$, the presence of a recirculation region leads to a weaker $\tau_{r\theta}$ distribution on the leeward side. On the other hand, at $Re = 50$, $s = 0.2$, the recirculation eddy is suppressed, and a strong flow gradient is created at the lower surface resulting in a larger and positive $\tau_{r\theta}$ contribution.

The persistent negative contribution from $\tau_{r\phi}$ is explained in figure 18. Contours of the local contribution to the viscous lift arising from $\tau_{r\phi}$, i.e. $-\tau_{r\phi}\sin\phi$, are shown for $Re = 200$, $s = 0.1$. A strong negative force acts over almost the entire surface. This downward force is generated by the distribution of the azimuthal velocity component, u_ϕ, around the sphere. Figure 18(b) shows the contours of the u_y velocity component on the (x, z)-plane. Note that in this plane u_ϕ is identical to u_y. The u_y component is directed towards the negative y-axis around the sphere over almost the entire (x, z)-plane, except near the rear stagnation point. The contours of u_y are clustered more closely on the upstream side than on the downstream side. As result a strong negative gradient is generated over the upstream side of the sphere, and a relatively weaker positive gradient is created over a smaller region on the downstream surface. Therefore, $-\tau_{r\phi}\sin\phi$ integrated over the entire surface leads to a negative contribution to the lift force.

4.2.4. *Effect of varying Θ*

The effect of varying the angle Θ is investigated in figure 19. We consider only the range $0 \leqslant \Theta \leqslant \pi/2$, and the results for $\pi/2 < \Theta < \pi$ can easily be obtained by the transformation $\Theta \rightarrow \Theta + \pi/2$. According to the potential flow result (4.9), the drag coefficient for such a configuration is given by $2s\cos 2\Theta$, and the lift coefficient

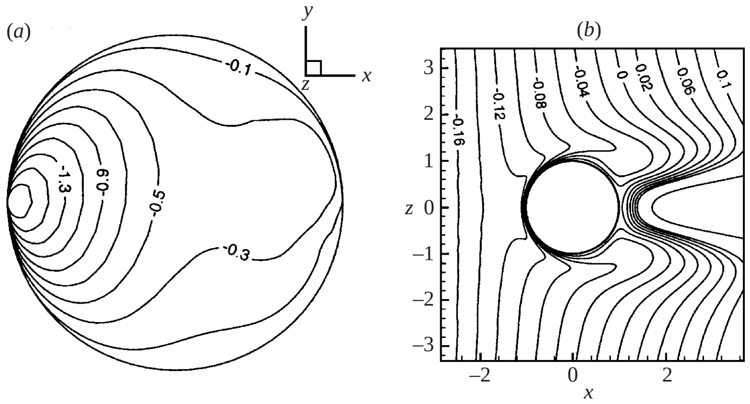

FIGURE 18. Viscous lift due to $\tau_{r\phi}$ at $Re = 200$, $s = 0.1$. (a) Contours of the y-component of viscous lift due to $\tau_{r\phi}$. (b) Contours of azimuthal velocity component u_ϕ in the (x, z)-plane.

(directed towards the positive y-direction) by $2s \sin 2\Theta$. These results are compared with the simulation results for the $Re = 10$, $s = 0.1$ and $Re = 50$, $s = 0.1$ cases. For both cases the trend of the pressure drag matches reasonably well with the potential flow result. For $\Theta < \pi/4$, the elongational part of the strain-rate tensor is more aligned with the direction of relative velocity and the drag coefficient is higher than in uniform flow. As Θ increases, the compressional part of the strain-rate tensor becomes more aligned with relative velocity and results in a decrease in C_D.

The lift coefficients for the two cases are shown in figures 19(b) and 19(c). The trend is somewhat complex and is dictated by the presence or absence of a recirculation eddy. The pressure contribution, C_{PL}, at $Re = 10$ is positive for all Θ with a maximum value at about $\Theta = \pi/4$ and thus follows the same trend as in potential flow. The viscous contribution C_{VL} is negative in the range $\pi/4 < \Theta < \pi/2$ due to a negative contribution from $\tau_{r\phi}$, as discussed earlier. However, the pressure contribution outweighs the viscous contribution, and the total lift force remains positive at $Re = 10$ for all Θ.

At $Re = 50$, in figure 19(c), we consider the range $0 \leqslant \Theta \leqslant 3\pi/8$, as $\Theta = \pi/2$ (pure compressional alignment) was found to be unstable (see §4.2.2). Unlike in potential flow, C_{PL} is not symmetric about $\Theta = \pi/4$, and it exhibits a peak around $\Theta = \pi/8$. Although positive in general, it tends to become negative at higher Θ where the compressional strain is increasingly aligned with relative velocity. Such behaviour is again due to the presence of a recirculation region. For $\Theta < \pi/8$, the recirculation region is suppressed, and the top–bottom asymmetry in the surface pressure leads to a positive C_{PL}. Above $\Theta = \pi/8$, a recirculation region starts developing which reduces the wake pressure difference above and below the (x, z)-plane, and the pressure differential near the front stagnation point dominates, leading to a negative pressure lift. The viscous lift coefficient at $Re = 50$ is negative over the entire range of Θ. For $\Theta > \pi/6$, its magnitude is higher than the pressure lift coefficient resulting in a negative total lift force.

4.2.5. *Relative velocity away from the plane of strain*

In this section we will consider a strain orientation such that the relative velocity is not on the plane of strain; in particular, the results for $\Theta = 0$ and $\Phi = \pi/4$ (figure 4d) are presented here. For an axisymmetric strain this configuration is the same as for

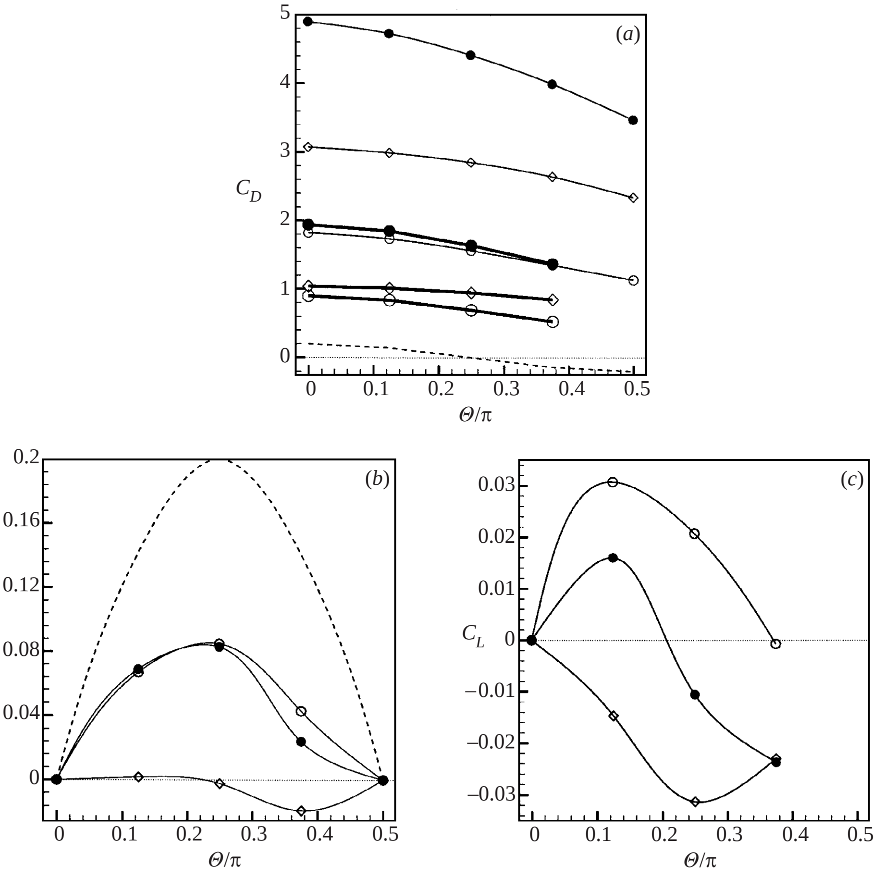

FIGURE 19. Effect of varying Θ on the drag and lift coefficients. Drag coefficients at (*a*) $Re = 10$, $s = 0.1$ (thin lines) and $Re = 50$, $s = 0.1$ (thick lines); –●–, C_D; –○–, C_{PD}; –◇–, C_{VD}. Lift coefficients at (*b*) $Re = 10$, $s = 0.1$ and (*c*) $Re = 50$, $s = 0.1$; –●–, C_L; –○–, C_{PL}; –◇–, C_{VL}. ----, Potential flow result.

$\Theta = \pi/4, \Phi = 0$. For a planar strain these two cases are very different in terms of the wake structure and the drag and lift forces. Here, the (x, z)-plane is a plane of symmetry, and streamlines constructed on this plane are shown in figure 20. Adjacent to the sphere, the ambient velocity is higher along $x = 0$, $z < 0$, and this side will be termed the high-speed side while $x = 0$, $z > 0$ will be called the low-speed side. A word of caution is warranted in interpreting this figure–although in the vicinity of the sphere the effect of strain appears to move the fluid from top left to bottom right, the far-field flow is consistent with what is shown in figure 4(*d*).

In figure 20(*a*), for $Re = 10$, $s = 0.1$, it is observed that the rear and front stagnation points move away from the geometric poles at $\theta = 0$ and π. The front stagnation point has moved towards the high-speed side, and the rear one has moved to the low-speed side. At $Re = 50$, $s = 0.05$, in figure 20(*b*), the wake is suppressed on the high-speed side and reduced in size on the low-speed side. As s is increased to 0.2 keeping Re fixed at 50, in figure 20(*c*), the wake is completely suppressed. The case of $Re = 300$, $s = 0.1$ is shown in figure 20(*d*). Suppression of the wake is now possible only at higher strain magnitudes. Comparing figure 20 with figure 12 it can be seen that the streamlines on the (x, z)-plane in the case of $\Theta = 0$, $\Phi = \pi/4$ appear qualitatively similar to those on

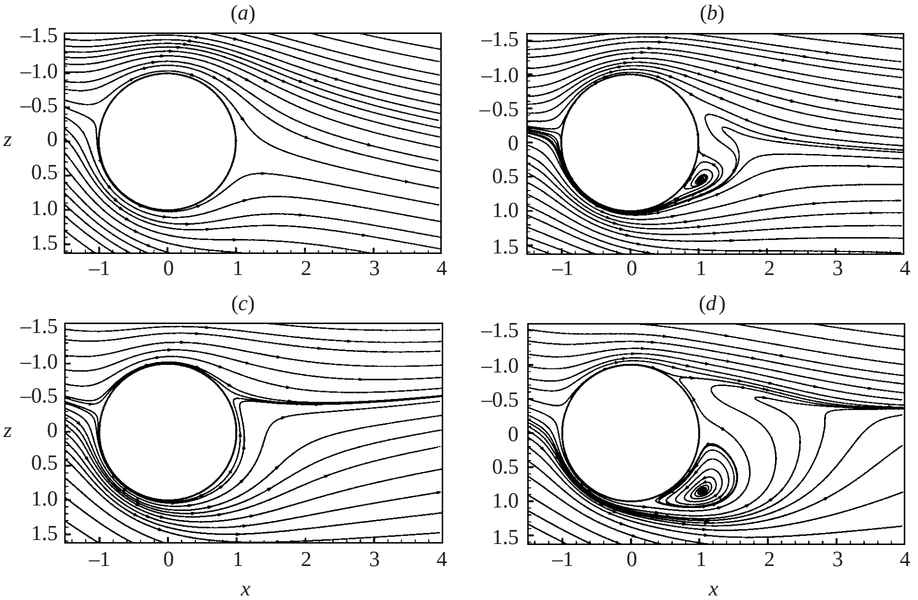

FIGURE 20. Streamline contours for $\Theta = 0$, $\Phi = 45°$ on the (x, z)-plane. (*a*) $Re = 10$, $s = 0.1$; (*b*) $Re = 50$, $s = 0.05$; (*c*) $Re = 50$, $s = 0.2$; (*d*) $Re = 300$, $s = 0.1$.

the (x, y)-plane in the case of $\Theta = \pi/4$, $\Phi = 0$. However, quantitative differences exist between the two cases, for example, in terms of the location of the separation points. In general, at the same Re and s, the deformation of the wake is less for $\Theta = 0$, $\Phi = \pi/4$ than for $\Theta = \pi/4$, $\Phi = 0$. This can be clearly seen for $Re = 300$, $s = 0.1$ by comparing figures 12(*d*) and 20(*d*).

The surface streamlines for the orientation $\Theta = 0, \Phi = \pi/4$ are shown in figure 21, and a qualitative comparison with figure 13 can be drawn. At $Re = 50$, $s = 0.05$, in figure 21(*a*), the axisymmetric nature of the wake is broken, and the rear stagnation point (denoted by RS in the figure) is seen to have shifted to the low-speed side. Two saddle points (S1 and S2) are seen on the separation line along the (x, z)-plane, while two nodal points (N1 and N2) appear on both sides of the (x, z)-plane on the high-speed side. When s is increased to 0.1, the asymmetry about the (x, y)-plane is further enhanced as in figure 21(*b*). A further increase in s to 0.2 causes the separation line to disappear on the low-speed side (figure 21*c*). The nodal points now have moved closer to the (x, z)-plane. The case of $Re = 300$, $s = 0.1$ is shown in figure 21(*d*). The separation line now appears as a closed curve, and the rear stagnation point has shifted to the high-speed side. On the symmetry plane, a saddle point (S) exists on the high-speed side and a nodal point (N) on the low-speed side.

The velocity potential for the configuration $\Theta = 0$, $\Phi \neq 0$ is given by

$$\left(\tilde{r} + \frac{1}{16\tilde{r}^2}\right)\cos\theta + s\left(\frac{\tilde{r}^2}{2} + \frac{1}{96\tilde{r}^3}\right)\left(\tfrac{3}{2}\cos^2\theta - \tfrac{1}{2}\right)\cos^2\Phi$$
$$-s\left(\frac{\tilde{r}^2}{4} + \frac{1}{192\tilde{r}^3}\right)[(\sin^2\theta\cos 2\phi)(1+\sin^2\Phi) + (\sin 2\theta\ \sin\phi)\sin 2\Phi]. \qquad (4.10)$$

For $\Phi = \pi/4$, the above equation yields $C_{D,\mathrm{pot}} = s$. The corresponding finite-*Re* results are shown in figure 22. At $s = 0.1$, C_D is slightly lower than the uniform flow result over the entire range of *Re*. The effect of increasing s at $Re = 50$ is also shown in the

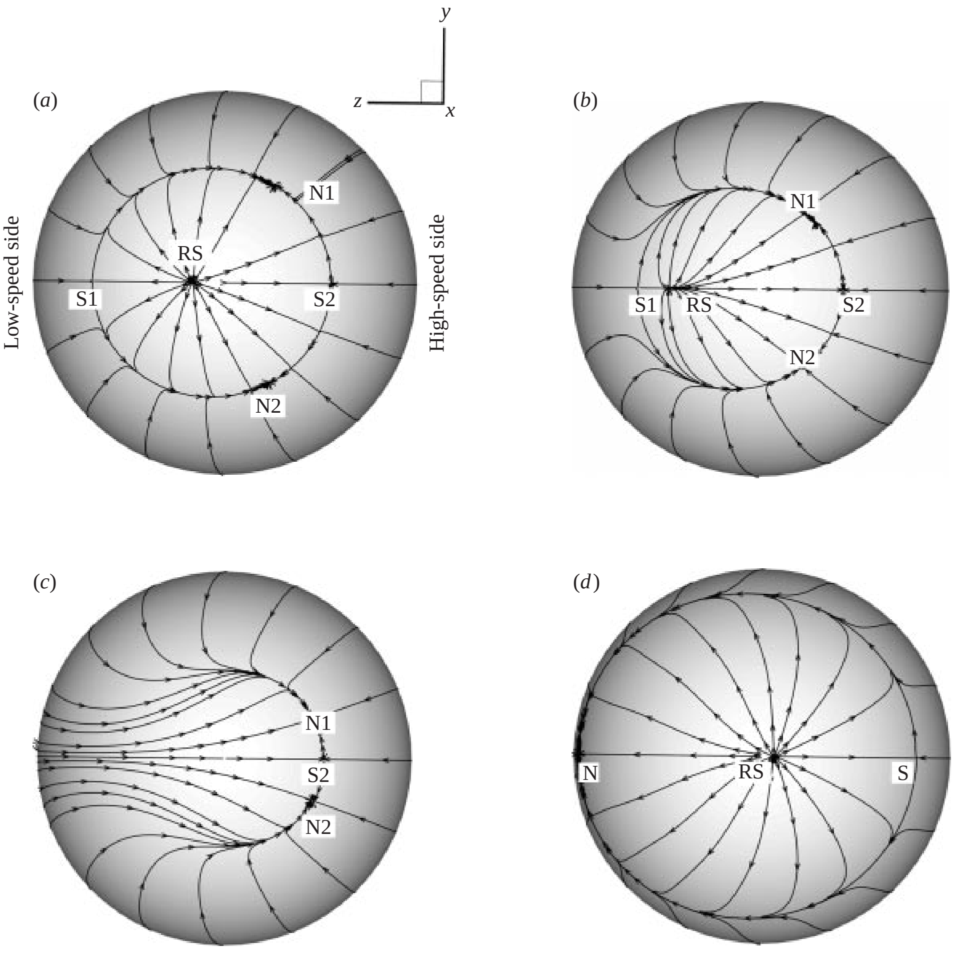

FIGURE 21. Surface streamlines for $\Theta = 0$, $\Phi = 45°$: (a) $Re = 50$, $s = 0.05$, (b) $Re = 50$, $s = 0.1$, (c) $Re = 50$, $s = 0.2$, (d) $Re = 300$, $s = 0.1$.

figure. Unlike the potential flow result, C_D at finite Re does not vary linearly with s. It reaches a minimum at around $s = 0.1$, and then slowly increases. At $s = 0.3$, C_D is about 26% higher than the uniform flow result. From the streamline plots shown in figure 20 it can be inferred that up to about $s = 0.1$, the presence of the recirculation region dictates the behaviour of drag; during this process the drag force decreases. With the further increase in strain, the recirculation region is suppressed, and the potential flow behaviour is mimicked somewhat.

Due to the asymmetry in the ambient flow about the (x, y)-plane, a side force is generated along the positive z-direction. This behaviour is different from the potential flow result, which predicts a side force of magnitude s, but directed along the negative z-direction. Here we will denote the side-force coefficients by C_Z, $C_{Z,P}$ and $C_{Z,V}$ representing the total, pressure and viscous components, respectively. Variations of these coefficients for the finite-Re case are shown in figure 23. When s is fixed at 0.1 and Re is varied, the coefficients are positive over the entire Re range. Although the flow field close to the sphere appears to be qualitatively similar to the case of the in-plane strain oriented at $\Theta = \pi/4$, $\Phi = 0$, by comparing figures 23 and 14, it can be

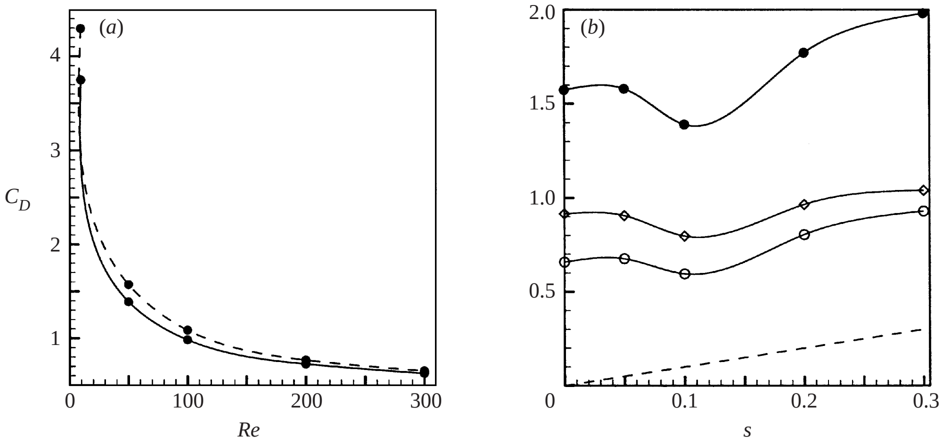

FIGURE 22. Drag coefficients for $\Theta = 0$, $\Phi = 45°$. Variation of (*a*) C_D with Re at $s = 0.1$. Dashed line is the uniform flow result. (*b*) Drag coefficients at $Re = 50$ and varying s: ●, C_D; ○, C_{PD}; ◇, C_{VD}. Dashed line is the potential flow result corresponding to $\Theta = 0$, $\Phi = 45°$.

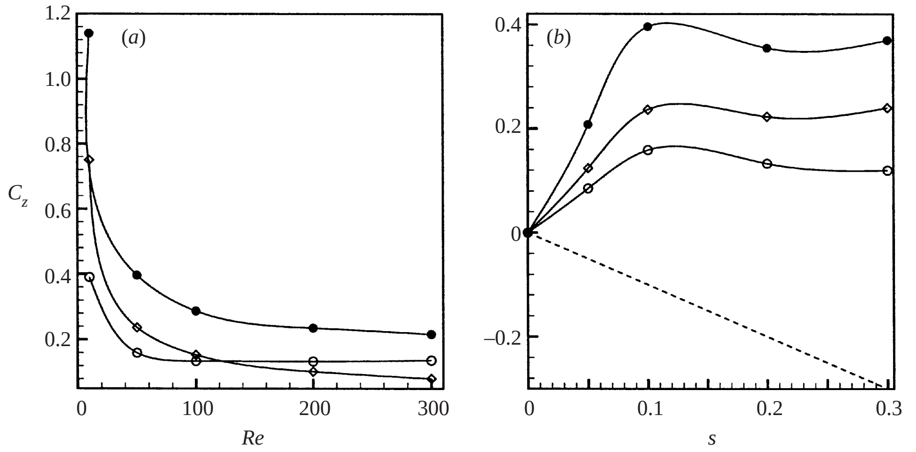

FIGURE 23. Side-force coefficients for $\Theta = 0$, $\Phi = 45°$. (*a*) $s = 0.1$, (*b*) $Re = 50$. ●, C_Z; ○, $C_{Z,P}$; ◇, $C_{Z,V}$. ----- potential flow result.

seen that the effect of strain orientation on lift is quite different. Most importantly, for the $\Theta = \pi/4$, $\Phi = 0$ case, the lift coefficient is an order of magnitude lower than the drag coefficient, whereas in figure 23, the side-force coefficient C_Z is significantly larger, and can be as high as 30% of C_D.

The variation of $\langle C_P \rangle$ with θ is shown in figure 24(*a*) for potential flow and for $Re = 50$. In potential flow, the asymmetry in $\langle C_P \rangle$ about $\theta = \pi/2$ increases with s contributing to a higher drag, whereas, at finite Re, the behaviour of drag is dictated by the presence or absence of a recirculation region in the wake. For $Re = 50$, $s \leqslant 0.1$, the presence of a recirculation region raises $\langle C_P \rangle$ on the downstream side which results in a lower drag compared to uniform flow. For $s > 0.1$, the recirculation region is suppressed, and $\langle C_P \rangle$ on the downstream side is reduced which results in a higher drag.

Figures 24(*b*) and 24(*c*) show the pressure contours on the surface of the sphere for potential flow at $s = 0.1$ and for $Re = 50$, $s = 0.1$. Asymmetry in the surface

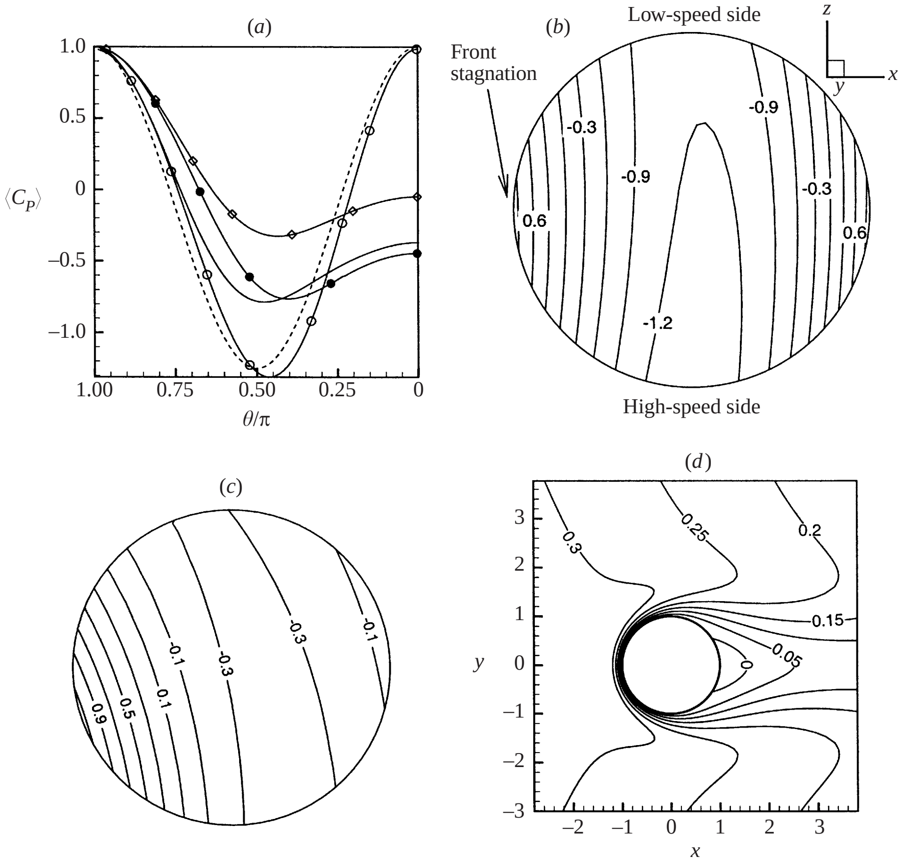

FIGURE 24. $\Theta = 0$, $\Phi = \pi/4$. (*a*) ϕ-averaged surface pressure coefficient: -----, potential flow at $s = 0$; —○—, potential flow at $s = 0.3$; ——, $Re = 50, s = 0$; —◇—, $Re = 50$, $s = 0.1$; —●—, $Re = 50$, $s = 0.3$. (*b*) Pressure contours in potential flow at $s = 0.1$. (*c*) Pressure contours for $Re = 50$, $s = 0.1$. (*d*) Contours of u_ϕ on the (x, y)-plane for $Re = 50, s = 0.1$.

pressure distribution about the (x, y)-plane is responsible for the z-force in both cases. The negative z-force in potential flow is primarily due to the dominant low pressure present on the high-speed side. No such distinct low-pressure region can be observed in figure 24(*c*). On the upstream side, in figure 24(*c*), pressure on the high-speed side is higher than on the low-speed side, while on the downstream side, pressure on the low-speed side is higher. The positive contribution coming from the upstream side outweighs the negative contribution from the downstream side, resulting in a positive side force.

Similarly to the pressure contribution, the viscous contribution to the z-force is also positive for the finite-Re cases. While both $\tau_{r\phi}$ and $\tau_{r\theta}$ contribute to the z-force, the former accounts for nearly 80%, and it is examined in figure 24(*d*) for $Re = 50$, $s = 0.1$. Here contours of the azimuthal velocity component u_ϕ are plotted on the (x, y)-plane, and the view shown is looking along the z-direction. Positive values of u_ϕ imply that it is directed from the plane of the paper into the positive z-direction. Except in the near-wake region, u_ϕ appears to be positive over the entire region around the sphere. Particularly, on the windward side, a strong positive gradient $\tau_{r\phi}$ exists which contributes positively to the viscous side force.

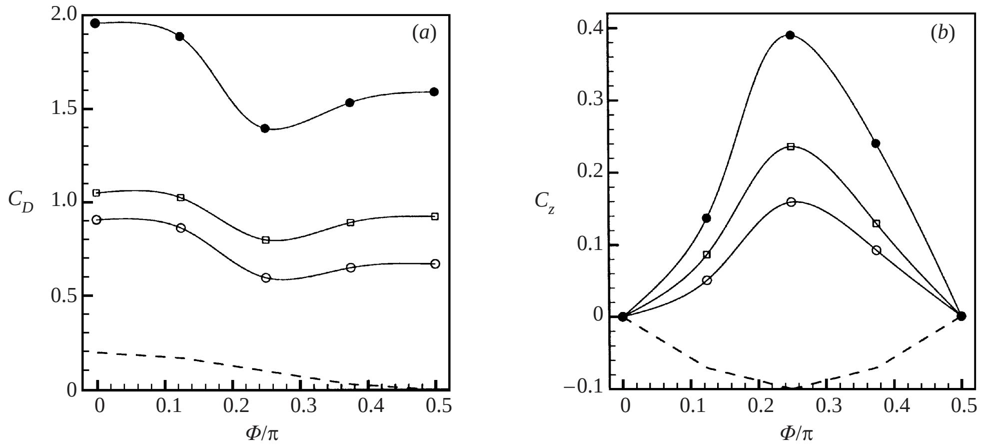

FIGURE 25. Effect of varying Φ. (*a*) Drag coefficients: ●, C_D; ○, C_{PD}; □, C_{VD}. (*b*) Side-force coefficients: ●, C_Z; ○, $C_{Z,P}$; □, $C_{Z,V}$. Data correspond to $Re = 50$, $s = 0.1$. Dashed line is the potential flow result at $s = 0.1$.

4.2.6. *Effect of Varying Φ*

Finally we consider the effect of varying the angle Φ between the relative velocity vector and the plane of strain. It is sufficient to consider the range $0 \leqslant \Phi \leqslant \pi/2$, and the results for $\pi/2 \leqslant \Phi \leqslant \pi$ can be obtained by the transformation $\Phi \rightarrow \Phi + \pi/2$. The drag and lift forces for varying Φ are shown in figure 25 for potential flow and for $Re = 50$ at $s = 0.1$. The potential flow solution (4.10) yields $C_{D,\mathrm{pot}} = 2s\cos^2\Phi$ and $C_{Z,\mathrm{pot}} = -s\sin 2\Phi$. The behaviour of the finite-*Re* drag and side-force coefficients are quite complex and markedly different from the potential flow results.

5. Conclusion

This paper is concerned with the effect of spatial non-uniformity in the undisturbed ambient flow on the forces acting on a spherical body. Using a simple scaling argument, it has been shown that the added-mass and pressure-gradient forces due to the particle acceleration can be neglected for heavy particles. However, when the particle size is comparable to the flow scales and the particle Reynolds number is of the order of unity or more, the added-mass and pressure-gradient terms arising from the fluid acceleration are important. In this paper we present results from the numerical simulations of a planar straining flow superimposed on a nominally steady uniform flow past a stationary sphere. The numerical methodology used in this study employs a high-resolution Fourier–Chebyshev pseudospectral scheme. The investigation covers a particle Reynolds number range of 10 to 300, thus extending from a non-separated wake to a time-dependent three-dimensional flow field. The planar straining flow is characterized by three parameters: the strain magnitude s, and the angles Φ and Θ formed between the relative velocity vector and the principal directions of the strain-rate tensor. A wide range of s, Θ and Φ is examined with a systematic comparison to the results of potential flow and finite-*Re* axisymmetric straining flow.

The focus has been to study the effect of planar strain on the structure of the wake in an attempt to explain the drag and lift forces acting on the particle. Several important observations can be made.

(*a*) Planar strain, when its axis of elongation is aligned with the direction of relative velocity, stabilizes the wake flow and delays the onset of unsteadiness. With increasing strain magnitude, separation is delayed and the length of the recirculation region decreases. Elongational strain of a sufficient magnitude completely suppresses the recirculating eddy. In this respect, both the planar and axisymmetric strains have a similar effect on the wake structure. Despite the three-dimensional nature of the planar strain, the separation line is nearly axisymmetric as indicated by the surface streamlines. Also, in terms of the length of the recirculation eddy and the angle of separation, the planar and axisymmetric strains yield similar results.

(*b*) Under the elongational alignment ($\Theta = 0$), both the planar and axisymmetric strain enhance the drag force. According to the potential flow theory, the strain-induced increase in drag is given by $2s$, and it is independent of the nature of the strain. In the case of axisymmetric strain, above a certain Re, the increase in pressure drag very nearly follows the potential flow prediction. In the case of planar strain, the increase in pressure drag is still linear with s, but the rate of increase is higher. In both the planar and axisymmetric strains, the viscous drag also increases with s, thus the increase in total drag is higher than the potential flow prediction. At low Re, the increase in viscous drag is higher for planar strain; however, for $Re \geqslant 50$, the viscous drag is nearly the same for both cases.

(*c*) In potential flow, strain introduces a fore–aft asymmetry about $\theta = \pi/2$, contributing to drag. At finite Re, the region of favourable pressure gradient extends into the leeward side of the sphere. Nevertheless, the wake pressure decreases, resulting in a further enhancement of the pressure drag. The drop in the wake pressure is higher for planar strain.

(*d*) There are two mechanisms by which the surface vorticity distribution is modified under the influence of strain, leading to an increase in the viscous drag. First, in addition to the uniform flow, the imposed straining flow must also satisfy the no-slip condition. This leads to an enhancement of the surface vorticity on the downstream side, and a reduction on the upstream side. Secondly, the vortex stretching mechanism also leads to a similar modification in the surface vorticity. The resultant effect is an increase in the viscous drag.

(*e*) When the compressional direction of strain is aligned with relative velocity ($\Theta = \pi/2$), the extent of the favourable pressure gradient on the upstream side is reduced, and the recirculation region increases in size. Both the pressure and viscous drag components decrease compared to the uniform flow result. Results for the compressional alignment cannot be extrapolated directly from those of the elongational alignment. The compressional alignment promotes unsteady vortex shedding in the wake, and even a modest magnitude of strain renders the flow highly unstable. The instability arises from the discontinuity in the vorticity distribution across a stagnation plane located downstream of the sphere.

(*f*) Planar strain oriented at an angle other than pure elongational or compressional alignment breaks the axisymmetric nature of the wake. The recirculation eddy is significantly deformed and the separation line, along with the associated critical points, on the surface of the sphere undergoes complex changes with increasing strain magnitude. For the case of $\Theta = \pi/4$, $\Phi = 0$ considered in detail, the recirculation region is completely suppressed at sufficiently high strain, and the strength of strain required for complete suppression increases with Re.

(*g*) For the $\Theta = \pi/4$, $\Phi = 0$ configuration, the drag force is nearly the same as in the uniform flow, in accordance with the potential flow result. However, unlike the potential flow where lift is always positive and increases linearly with the strain magnitude, at finite Re the lift force shows a non-monotonic behaviour and can be negative. The negative lift force can be related to the presence of a recirculation region in the wake. At higher strain magnitudes, when the recirculation region is suppressed, the potential flow behaviour is approximately recovered and the lift force becomes positive.

(*h*) The out-of-plane strain orientation $\Theta = 0$, $\Phi = \pi/4$ is found to yield markedly different results from the in-plane orientation $\Theta = \pi/4$, $\Phi = 0$ in terms of the flow structure and forces. In the case of axisymmetric strain these two configurations are identical. The drag force is higher than the uniform flow result but not linear with s as predicted by the inviscid theory. For the $\Theta = 0$, $\Phi = \pi/4$ orientation, the symmetry of the flow is broken, and as a result there is a side force. The side force is opposite in sign to that predicted by the potential theory, and its variation with strain magnitude is not linear.

(*i*) In general, for varying Θ and Φ, the present results show that at low *Re* (e.g. $Re \approx 10$) and for high strain magnitude in the absence of a recirculation eddy, the finite-*Re* drag and lift forces follow somewhat the pattern observed in potential flow. At higher Reynolds numbers, their behaviour is dictated by the presence of an eddy and thus may be very complex in nature.

The research is supported by the ASCI Center for Simulation of Advanced Rockets at the University of Illinois at Urbana-Champaign under the auspices of the US Department of Energy through the University of California subcontract number B341494. Computational facilities from the National Center for Supercomputing Applications, UIUC are greatly acknowledged. Special thanks are due to Drs J. P. Ferry and F. M. Najjar.

REFERENCES

Achenbach, E. 1974 Vortex shedding from spheres. *J. Fluid Mech.* **62**, 209–221.

Ashurst, W. T., Kerstein, A. R., Kerr, R. M. & Gibson, C. H. 1987 Alignment of vorticity and scalar gradient with strain rate in simulated Navier–Stokes turbulence. *Phys. Fluids* **30**, 2343.

Asmolov, E. S. 1999 The inertial lift on a spherical particle in a plane Poiseuille flow at large channel Reynolds number. *J. Fluid Mech.* **381**, 63–87.

Auton, T. R., Hunt, J. C. R. & Prud'homme, M. 1988 The force exerted on a body in inviscid unsteady non-uniform rotational flow. *J. Fluid Mech.* **197**, 241–257.

Balachandar, S. 1992 Structure in turbulent thermal convection. *Phys. Fluids* A **4**, 2715–2726.

Bedeaux, D. & Rubi, J. M. 1987 Drag on a sphere moving slowly through a fluid in elongational flow. *Physica* **144A**, 285–298.

Clift, R., Grace, J. R. & Weber, M. E. 1978 *Bubbles, Drops and Particles*. Academic.

Dandy, D. S. & Dwyer, H. A. 1990 A sphere in shear flow at finite Reynolds number: effect of shear on particle lift, drag and heat transfer. *J. Fluid Mech.* **216**, 381–410.

Dennis, S. C. R. & Walker, J. D. A. 1971 Calculation of the steady flow past a sphere at low and moderate Reynolds numbers. *J. Fluid Mech.* **48**, 771–789.

Elghobashi, S. E. & Truesdell, G. C. 1992 Direct simulation of particle dispersion in decaying isotropic turbulence. *J. Fluid Mech.* **242**, 655.

Gatignol, R. 1983 The Faxen formulae for a rigid particle in an unsteady non-uniform Stokes flow. *J. Mec. Theor. Appliqu.* **1**, 143–160.

Herron, I. H., Davis, S. H. & Bretherton, F. P. 1975 On the sedimentation of a sphere in a centrifuge. *J. Fluid Mech.* **68**, 209–234.

Hogg, A. J. 1994 The inertial migration of non-neutrally buoyant spherical particles in two-dimensional shear flows. *J. Fluid Mech.* **272**, 285–318.

Johnson, T. A. & Patel, V. C. 1999 Flow past a sphere up to a Reynolds number of 300. *J. Fluid Mech.* **378**, 19–70.

Kim, I., Elghobashi, S. & Sirignano, W. A. 1998 On the equation for spherical–particle motion: effect of Reynolds and acceleration numbers. *J. Fluid Mech.* **367**, 221–254.

Kurose, R. & Komori, S. 1999 Drag and lift forces on a rotating sphere in a linear shear flow. *J. Fluid Mech.* **384**, 183–206.

Le Clair, B. P., Hamielec, A. E. & Pruppracher, H. R. 1970 A numerical study of the drag on a sphere at low and intermediate Reynolds numbers. *J. Atmos. Sci.* **27**, 308–315.

Lovalenti, P. M. & Brady, J. F. 1993 The force on sphere in a uniform flow with small-amplitude oscillations at finite Reynolds number. *J. Fluid Mech.* **256**, 607–614.

Magarvey, R. H. & Bishop, R. L. 1961 Transition ranges for three-dimensional wakes. *Can. J. Phys.* **39**, 1418–1422.

Magnaudet, J. & Eames, I. 2000 The motion of high-Reynolds number bubbles in inhomogeneous flows. *Annu. Rev. Fluid Mech.* **32**, 659–708.

Magnaudet, J., Rivero, M. & Fabre, J. 1995 Accelerated flows past a rigid sphere or a spherical bubble. Part 1. Steady straining flow. *J. Fluid Mech.* **284**, 97–135.

Maxey, M. R. & Riley, J. J. 1983 Equation of motion for a small sphere in a nonuniform flow. *Phys. Fluids* **26**, 883–889.

McLaughlin, J. B. 1991 Inertial migration of a small sphere in linear shear flows. *J. Fluid Mech.* **224**, 261–274.

McLaughlin, J. B. 1993 The lift on a small sphere in wall-bounded linear shear flows. *J. Fluid Mech.* **246**, 249–265.

Mei, R. 1990 Particle dispersion in isotropic turbulence and unsteady particle dynamics at finite Reynolds number. PhD thesis, University of Illinois at Urbana-Champaign, Urbana, IL.

Mei, R. & Adrian, R. J. 1992 Flow past a sphere with an oscillation in the free-stream and unsteady drag at finite Reynolds number. *J. Fluid Mech.* **237**, 133–174.

Merilees, P. E. 1973 A pseudospectral approximation applied to the shallow water equation on a sphere. *Atmosphere* **11**, 13–20.

Mittal, R. 1999 A Fourier Chebyshev spectral collocation method for simulation flow past spheres and spheroids. *Intl J. Numer. Meths. Fluids* **30**, 921–937.

Mittal, R. & Balachandar, S. 1996 Direct numerical simulation of flow past elliptic cylinders. *J. Comput. Phys.* **124**, 351–367.

Natarajan, R. & Acrivos, A. 1993 The instability of the steady flow past spheres and disks. *J. Fluid Mech.* **254**, 323–344.

Orszag, S. A. 1974 Fourier series on spheres. *Mon. Weather Rev.* **102**, 56–75.

Pérez-Madrid, A., Rubí, J. M. & Bedeaux, D. 1990 Motion of a sphere through a fluid in stationary homogeneous flow. *Physica* A **163**, 778–790.

Saffman, P. G. 1965 The lift on a small sphere in a slow shear flow. *J. Fluid Mech.* **22**, 385–400 (and Corrigendum, **31**, 1968, 624).

Sakamoto, H. & Haniu, H. 1990 A study on vortex shedding from spheres in a uniform flow. *Trans. ASME: J. Fluids Engng* **112**, 386–392.

Sakamoto, H. & Haniu, H. 1995 The formation mechanism and shedding frequency of vortices from a sphere in uniform shear flow. *J. Fluid Mech.* **287**, 151–171.

Shariff, K. 1993 Comment on "Coordinate singularities" by P. R. Spalart. Unpublished.

Squires, K. D. & Eaton, J. K. 1991 Measurements of particle dispersion from direct numerical simulations of isotropic turbulence. *J. Fluid Mech.* **226**, 1–35.

Stone, H. A. 2000 Philip Saffman and viscous flow theory. *J. Fluid Mech.* **409**, 165–183.

Taylor, G. I. 1928 The forces on a body placed in a curved or converging stream of fluid. *Proc. R. Soc. Lond.* A **120**, 260.

Tobak, M. & Peake, D. J. 1982 Topology of three-dimensional separated flows. *Annu. Rev. Fluid Mech.* **14**, 61–85.

Tollmien, W. 1938 Uber krafte und momente in schwach gekrummten oder konvergenten stromungen. *Ing. -Arch.* **9**, 308.

Tomboulides, A. G., Orszag, S. A. & Karniadakis, G. E. 1993 Direct and large-eddy simulation of axisymmetric wakes. *AIAA Paper* 93-0546.

Voinov, V. V., Voinov, O. V. & Petrov, A. G. 1973 Hydrodynamic interactions between bodies in a perfect incompressible fluid and their motion in non-uniform streams. *Prikl. Math. Mekh.* **37**, 680.

Wang, L.-P. & Maxey, M. R. 1993 Settling velocity and concentration distribution of heavy particles in homogeneous isotropic turbulence. *J. Fluid Mech.* **256**, 27–68.

Weisenborn, A. J. 1985 Drag on a sphere moving slowly in a rotating viscous fluid. *J. Fluid Mech.* **153**, 215–227.

Yee, S. Y. K. 1981 Solution of Poisson's equation on a sphere by truncated double Fourier series. *Mon. Weather Rev.* **109**, 501–505.

Zhou, J., Adrian, R. J., Balachandar, S. & Kendall, T. M. 1999 Mechanism for generating coherent packets of hairpin vortices in near wall turbulence. *J. Fluid Mech.* **387**, 353–396.